

# Numerical investigation of viscous flow instabilities through heterogeneous porous media. Advantages and limitations of unstructured and adaptive meshes in 2D and 3D domains under different mobility scenarios.

K. Christou<sup>a</sup>, W.C. Radünz<sup>a,b</sup>, B. Lashore<sup>a</sup>, F.B.S. de Oliveira<sup>c</sup>, J.L.M.A. Gomes<sup>a,\*</sup>

<sup>a</sup>*Environmental and Industrial Fluid Mechanics Group, School of Engineering,  
University of Aberdeen, UK*

<sup>b</sup>*Engineering School, Federal University of Rio Grande do Sul, Brazil*

<sup>c</sup>*Department of Exact and Technological Sciences, State University of Santa Cruz,  
Bahia, Brazil*

---

## Abstract

The aim of this paper is to model flow instabilities *i.e.*, viscous fingering using a novel method for modeling multi-phase flows in heterogeneous porous with either uniform or random generated permeability distribution. Starting from modelling the Hele-Shaw experimental apparatus, which is mathematically analogous to the two-dimensional flow in porous media problem. The development of finger structures is investigated by taking into account different conditions such as, different domains under uniform or different permeabilities regions, mobility ratios, mesh types. A novel control finite element method (CVFEM) is used to discretize the governing equations that will solve the multi-fluid porous media flow model. The governing multiphase porous media flow equations are solved using an unstructured mesh by introducing adaptivity in later stages. Dynamic mesh adaptivity will not only help to better capture the development of finger but also allow the system to focus the computational effort where is needed, minimizing both the CPU time and the numerical diffusion. It was found that mobility ratio along with the initial and boundary conditions, as well as the use of adaptivity on top

---

\*Corresponding author.

Email address: [jefferson.gomes@abdn.ac.uk](mailto:jefferson.gomes@abdn.ac.uk) (J.L.M.A. Gomes)

of an unstructured mesh allow the user to better describe and visualise the phenomenon.

*Keywords:* Multi-fluid flows, Porous media, Viscous Instabilities, Mobility Ratio, Preferential flowpath, Finite Element Methods, Capillary number, Unstructured domain, Mesh adaptivity.

---

## 1. Introduction

Numerical investigation of multiphase flows in porous media have attracted the attention of the scientific community over the past 40 years. Characterisation of such fluid flows serves as the foundation of reservoir engineering and groundwater studies (White et al., 1981). Underground coal gasification is another important field of interest and, more recently, due to global environmental problems, several research work has been focused on CO<sub>2</sub> migration and trapping mechanisms in carbon capture utilisation and storage (CCUS) operations (Spycher et al., 2003; Self et al., 2012; Jiang, 2011).

Description of physics and mechanisms of multiphase flows were reported by Wooding and Morel-Seytoux (1976) with focus on capillary pressure and flow regimes. A comprehensive review of mechanisms of fluid instabilities (*i.e.*, fingering) and forces acting on the interface between two immiscible fluids can be found in Homsy (1987). Adler and Brenner (1988) described both microscopic and macroscopic scale Darcy-equations. The first distinction should be made between microscopic and macroscopic instabilities. Microscopic instabilities describe phenomena occurring locally, for example, Kelvin-Helmholtz and Saffman-Taylor instabilities (Saffman, 1959). On the other hand, macroscopic instabilities involve two-phase flow system (Bottino and Sengpiel, 1992). This paper focuses on microscopic instabilities in two-phase systems that occurs due to viscous and stress forces, often referred as viscous instabilities or *viscous fingering* (see section 3).

In oil and gas reservoir exploration, viscous and density instabilities are relatively common during water-injection processes. As water and oil interacts, the interface between these two fluids moves creating an uneven or fingered flow profile (see Fig. 3). Viscous fingering results in inefficient flow sweeping which can bypass significant quantities of recoverable oil and, may lead to early breakthrough of water into neighbour production wells. Viscous instabilities are mainly governed by the mobility ratio (MR) between the displacing and the displaced fluids. Other conditions that may also influence the severity of viscous fingering are: heterogeneity (*i.e.*, wide spatial permeability distribution), gravitational forces, anisotropic dispersion, non-monotonic viscosity profile etc.

Conservation of mass and Darcy's law are the governing equations that describe flow dynamics in porous media. Advanced numerical methods are

in continuous development to accurately represent force balances in Darcian flows. Finite difference methods (FDM) have been extensively used in most industry-standard reservoir simulators ([Aziz and Settari, 1986](#); [Chen et al., 2005](#); [Chang et al., 1990](#)) with relative success. However, they are often limited to relatively simple geometries representing idealised geological formations through structured quadrilateral (2-D) and hexahedral (3-D) grid cells of low quality ([Mlacnik et al., 2004](#); [King and Mansfield, 1999](#)). Additionally, FDM produce excessive numerical dispersion when heterogeneity (represented by permeability and porosity fields) is present ([Chavent and Jaffré, 1986](#)).

The geometrical flexibility associated with high-order numerical accuracy of finite element methods (FEM) has proven to be more efficient than FDM schemes when they are used to solve complex geometries. Among FEM-based formulations for porous media, the control volume finite element methods (CVFEM, [Fung et al., 1992](#)) has been largely used as it can guarantee local mass conservation and high-order numerical accuracy as well as being able to use tetrahedral geometry-conforming elements. In traditional CVFEM formulations, pressure and velocity are interpolated using piecewise linear FE basis functions, while material properties and flow conditions (*e.g.*, phase saturation, density, temperature, species concentration etc) are represented with CV basis functions ([Voller, 2009](#)). Saturation equations are solved explicitly after solving for the dual pressure-velocity at each non-linear iteration (a detailed description of the implicit pressure explicit saturation, IMPES, formulation can be found in [Chen et al., 2006](#); [Lux and Anguy, 2012](#)).

Since geometries are captured by finite elements, constructed control volumes typically extend on each side of the interface which may have different properties. Therefore, some average values of the coupled velocity-pressure fields (defined in the FE space but projected into the CV space) are applied across the CVs at these interfaces. These often lead to excessive numerical dispersion especially in highly heterogeneous media (represented by spatial-dependent permeability and porosity fields). In order to overcome such artificial numerical dispersion, a discontinuous hybrid finite element finite volume method (DFEFVM) was introduced by [Nick and Matthai \(2011a,b\)](#). This novel discretisation scheme was designed to simulate flows through discrete fractured rocks in which CVs are divided along the interfaces of different materials. [Cumming et al. \(2011\)](#) demonstrated that CVFEM discretisation

could also be used to solve Richards' equations (coupled mass conservation and Darcy equation) in heterogeneous media with relatively small computational overhead (compared with traditional coupled velocity-pressure based formulations, see also Cumming, 2012). Fluxes over CVs were calculated based upon material properties, whereas the saturation field was volume-averaged at the interface of the materials, enforcing mass balance as described by Kirkland et al. (1992).

In this work, a novel CVFEM formulation, previously introduced by Gomes et al. (2017)(see also Jackson et al., 2014; Salinas et al., 2015), is used to conduct numerical investigation of formation and evolution of viscous fingers in heterogeneous media. The continuity equation is embedded into the pressure equation to enforce mass conservation whilst ensuring force balance is preserved. A hybrid family of  $P_n$ DG- $P_m$  triangular and tetrahedral FE pairs is used to discretise velocity and pressure, in which velocity is represented by  $n$  th-order polynomials that are discontinuous across elements whereas pressure is represented by  $m$  th-order polynomials that are continuous across the elements. A sketch of a  $P_1$ DG- $P_2$  FE-pair is shown in Fig. 1, in which velocity is represented by discontinuous and piecewise linear basis functions whereas pressure is interpolated through continuous and piecewise quadratic basis functions. Scalar fields are stored in CV space (Fig. 2). The dual pressure and velocity fields are represented simultaneously (through non-linear projections) in FE and CV spaces.

A brief description of the numerical formulation and viscous fluid instabilities are introduced in Sections 2 and 3, respectively. Model set up and results including initial model-benchmark are presented in Section 4. Impact of mobility ratio on the fingers formation is also included in this section. Finally, concluding remarks are presented in Section 5.

## 2. Model Formulation

The two-phase immiscible and incompressible fluid flow through a porous media domain  $\Omega$ , may be described by the coupled extended Darcy and saturation equations,

$$\left( \frac{\mu_\alpha S_\alpha}{\mathbf{K} \mathcal{K}_{r\alpha}} \right) \mathbf{u}_\alpha = \underline{\underline{\sigma}}_\alpha \mathbf{u}_\alpha = -\nabla p + \mathcal{S}_{u,\alpha}, \quad x_i \in \Omega, t > 0 \quad (1)$$

$$\phi \frac{\partial S_\alpha}{\partial t} + \nabla \cdot (\mathbf{u}_\alpha S_\alpha) = \mathcal{S}_{cty,\alpha}, \quad x_i \in \Omega, t > 0 \quad (2)$$

respectively, where  $\mu$ ,  $\mathbf{K}$ ,  $p$  and  $\phi$  are viscosity, absolute permeability, pressure and porosity, respectively.  $\mathbf{u}_\alpha$  is the saturation-weighted Darcy velocity of the  $\alpha$ -phase and  $\mathcal{K}_{r,\alpha}$  is the relative permeability.  $\mathcal{S}$  is the source term associated with the Darcy and continuity equations.  $S_\alpha$  represents the saturation of the  $\alpha$ -phase with mass conservation constraints of

$$\sum_{\alpha=1}^{\mathcal{N}_p} S_\alpha = 1,$$

where  $\mathcal{N}_p$  denotes the number of phases.

Finite element basis functions for velocity and pressure fields are introduced in the discretisation of force-balance equation (Eqn. 1). Hybrid basis functions are also used to allow CV-based velocity to be extrapolated across the entire element.  $\underline{\underline{\sigma}}_\alpha$  is an absorption-like term that represents the implicit linearisation of the viscous frictional forces, and lies in both CV and FEM spaces.

Whilst saturation (and all saturation-dependent material properties such as relative permeability and capillary pressure) is calculated in CV space, permeability is piecewise constant in FE space. Saturation equations (Eqn. 2) are discretised in space with CV basis function and with the  $\theta$ -method in time as described by [Gomes et al. \(2012\)](#). Velocities across CV interfaces (within and between elements) are calculated through a directional-weighted flux-limited scheme based on upwind value of  $\sigma$  at individual CV as described by [Jackson et al. \(2013\)](#).

This formulation is applicable to  $\mathcal{N}_p$  fluid phases and is based on two families of FE-pairs:  $P_n$ DG- $P_m$ DG and  $P_n$ DG- $P_m$  ([Cotter et al., 2009](#)), consistent with the dual pressure-velocity representation in control volume (CV). In these families of FE-pairs velocity is represented by  $n^{\text{th}}$ -order polynomials that are discontinuous across elements, whereas pressure is represented by  $m^{\text{th}}$ -order polynomials that may be either continuous or discontinuous

(thus the notation  $P_n$ DG- $P_m$  and  $P_n$ DG- $P_m$ DG, respectively) across elements. Mass balance (continuity) equations are solved in CV space and a Petrov-Galerkin FEM is used to obtain high-order fluxes on CV boundaries, which are limited to yield bounded fields. Simulations performed for this work were conducted using two types of elements:  $P_1$ DG- $P_2$  and  $P_1$ DG- $P_1$ . Equation 2 is discretised in time and space using the  $\theta$ -method. Summing over all phases yields the global mass balance equation,

$$\sum_{\alpha=1}^{N_p} \left\{ \int_{\Omega_{CVi}} M_i \frac{\phi (S_{\alpha i}^{n+1} - S_{\alpha i}^n)}{\Delta t} dV + \oint_{\Gamma_{CVi}} [\theta^{n+1/2} \mathbf{n} \cdot \mathbf{u}_{\alpha}^{n+1} S_{\alpha}^{n+1} + (1 - \theta^{n+1/2}) \mathbf{u}_{\alpha}^n S_{\alpha}^n] d\Gamma - \int_{\Omega_{CVi}} M_i \mathcal{S}_{cty,\alpha}^{n+\theta} dV \right\} = 0, \quad (3)$$

where  $\Omega_{CVi}$  and  $\Gamma_{CVi}$  are the volume and boundary of CV  $i$  respectively,  $M_i$  are CV basis functions,  $\mathbf{n}$  is the outward pointing unit normal vector to the surface of  $CV_i$  and  $n$  is the current time level.  $\theta$  varies smoothly between 0.5 (corresponding to Crank-Nicolson method) and 1 (corresponding to backward-Euler scheme) to avoid the introduction of spurious oscillations for large grid Courant numbers. In addition to the numerical schemes above the discretised global mass and force balance equations are solved using a multigrid-like approach (see Pavlidis et al., 2016). This numerical formulation is fully described by Gomes et al. (2017)(see also Salinas et al., 2015; Adam et al., 2016).

### 3. Brief Summary of Viscous Instabilities

Flow instabilities may be due to pressure gradient along the interface of fluids, stress forces acting in opposite directions, mobility differences that may exceed critical limits and heterogeneities of the domain. When the driving force of the injected fluid overcomes the capillary force, hydrodynamic instabilities may occur, resulting in the collapse of the interface between fluids and start forming fingers.

Viscous instabilities (*i.e.*, fingering) can become more pronounced due to heterogeneities (*i.e.*, natural fractures, different permeability characteristics

in different zones) of the porous medium therefore sweep efficiency may be reduced or early breakthrough may occur (Riaz and Tchelepi, 2004; Tavassoli et al., 2015). During immiscible CO<sub>2</sub> flooding, density of supercritical CO<sub>2</sub> is usually lower than the *in situ* hydrocarbons, thus viscous fingering and/or channelling may occur.

As mentioned above viscous flow instabilities can be found across many research areas, disciplines and scales, from chemical and medical separation systems to large scale geological reservoir fields. Muskat (1934) investigated the flow of a fluid injected between two infinite parallel plates and the impact of capillary number ( $N_c$ ),

$$N_c = \frac{\mu U}{\gamma}, \quad (4)$$

In Eqn. 4,  $\mu$  is the viscosity of the fluid that initially fills the Hele-Shaw cell,  $\gamma$  is the surface tension and  $U$  is a velocity characteristic of the moving interface.

In the Hele-Shaw cell, a fluid is introduced between two parallel flat plates separated by an infinitesimally small gap. This experimental apparatus allows the predicted instability to be verified qualitatively and simplifies the problem of flow in both porous and non-porous media. More recently, Howison (2000) and Praud and Swinney (2005) gave a comprehensive description of the mathematical formulation of immiscible two-phase flows in Hele-Shaw cell (also known as Saffman & Taylor problem). For a Hele-Shaw cell of a given size the developing flow only depends on the capillary number. Thus if  $N_c$  is too high Saffman (1959), Homsy (1987), Tabeling et al. (1987) and others agreed that the flow develops into a single steady-state finger which moves through the cell with constant velocity  $U$ .

Under the assumption that fluids remain immiscible along an interface, surface tension plays an important role in determining the shape and progress of the fingers (Howison, 2000). During the displacement of a fluid by a less viscous one, the expected uniform front is perturbed leading to an uneven front with elongations of the outside edge of the fluid interface (Fig. 3), often referred as *fingers*. In homogeneous domains, fingers start to develop when the surface tension acting on the interface between the fluids exert an opposite force towards the change of shape of the interface. The interface becomes unstable and collapses, taking a curved shape.

In heterogeneous domains, such instability may also be triggered by permeability differences across regions as demonstrated in Section 4.3. The higher the velocity of the low viscosity fluid, the less wide (tip-splitting behaviour) the finger is. Pressure differences acting on the interface produces a net pressure force,

$$\Delta P = -\gamma \nabla \cdot \hat{n}. \quad (5)$$

This expression is also known as the Young-Laplace equation, a relation describing the capillary pressure across the interface between two fluids. With  $\Delta P$  denoting the pressure difference and  $\hat{n}$  is the unit normal vector out of the surface.

As demonstrated by [Habermann \(1960\)](#), *mobility ratio* (MR) is a key-parameter to assess fluid displacement and is defined as the ratio of mobility of the displacing (fluid  $i$ ) to that of the displaced fluid ( $j$ ),

$$MR = \frac{\mathcal{K}_{ri} \mu_j}{\mathcal{K}_{rj} \mu_i}. \quad (6)$$

MR is a function not only of fluids' viscosity and saturation, but also of the parameterised relative permeability,  $\mathcal{K}_{r\alpha}$ , which is often expressed as a function of the residual and maximum phase saturation prescribed in the pore rock matrix. In the simulations conducted for this work, the modified Brooks-Corey model was used ([Alpak et al., 1999](#); [Brooks and Corey, 1964](#)),

$$\mathcal{K}_{rw}(S_w) = \mathcal{K}_{rw}^o \left[ \frac{S_w - S_{w,irr}}{1 - S_{w,irr} - S_{nw,r}} \right]^{n_w}, \quad (7)$$

$$\mathcal{K}_{rnw}(S_w) = \mathcal{K}_{rnw}^o \left[ \frac{S_{nw} - S_{nw,r}}{1 - S_{w,irr} - S_{nw,r}} \right]^{n_{nw}}, \quad (8)$$

where subscripts  $w$  and  $nw$  stand for wetting and non-wetting phases, respectively.  $\mathcal{K}_{rw}^o$  and  $\mathcal{K}_{rnw}^o$  are end-point relative permeability to wetting and non-wetting phases,  $S_{w,irr}$  and  $S_{nw,r}$  are irreducible wetting and residual non-wetting phase saturations, respectively. Exponents  $n_w$  and  $n_{nw}$  are both set to 2.

From Eqns. 6-8, it is clear that during fluid displacement, the mobility ratio changes as phase saturation,  $S_w(x_i, t)$  and  $S_{nw}(x_i, t)$ , varies in time and space

(Eqn. 2). Therefore, with no lack of generality, the MR can be reduced to the viscosity ratio (VR),

$$\text{VR} = \frac{\mu_i}{\mu_j},$$

that will be used in the parametrisation of the numerical simulations conducted in Section 4. Analysis performed in the following sections will make use of this simplified definition as phase saturation is a prognostic field which is calculated along with pressure and velocity.

In immiscible displacements, viscous fingering occurs when the viscosity ratio is greater than unity. As surface tension becomes weak, the interface is stressed and becomes unstable leading to the formation of fingers. The interface collapses and starts splitting into new lobes of fingers. One of the fingers may eventually outgrow the others and then spreads to occupy an increasingly larger width. In the process, the finger reaches a (critical) width that is again unstable and splits again, and the pattern repeats itself. Thus, surface tension plays an essential dual role, it must be weak enough for the tip front to be unstable, but it is also the physical force causing the *spreading* and ensuing repeated branching.

In the next section, multi-fluid simulations are performed to numerically investigate: (a) the impact of heterogeneity (here represented by spatially-dependent permeability) on the onset and propagation of viscous instabilities in Sections 4.3 and 4.4; (b) the collapse of fluid interfaces through the use of adaptive mesh grid in Section 4.3; (c) the impact of viscosity ratios on the formation and progress of fingers in Section 4.4 and ??.

## 4. Results

### 4.1. Model Set-up

Numerical simulations were conducted with the model summarised in Section 2 and embedded in the next-generation reservoir simulator Fluidity/IC-FERST model software<sup>1</sup> (a full description of the model can be found in AMCG, 2012, 2010; Jackson et al., 2013; Gomes et al., 2017). This multi-physics model has been validated against traditional multi-fluids test-cases

---

<sup>1</sup><http://multifluids.github.io>

(*e.g.*, advection-diffusion, Buckley-Leverett problem, channel model, immiscible displacement, gravity-driven displacement etc) in Radünz et al. (2014); Jackson et al. (2014); Salinas et al. (2015); Pavlidis et al. (2016).

All test-cases were performed in idealised geometries discretised with unstructured triangular mesh using the P<sub>1</sub>DG-P<sub>2</sub> and P<sub>1</sub>DG-P<sub>1</sub> FE-pairs. An implicit Crank-Nicolson time-stepping scheme was used with an *a posteriori* adaptive time-step size targeting a maximum Courant-Friedrichs-Lowy (Courant et al., 1941) number of 2. In most simulations, the domain was initially fully saturated with non-wetting fluid which was displaced by a pure (wetting) fluid at a prescribed initial velocity ( $u^0$ ). For simplicity, the porosity ( $\phi$ ) of the domain was kept constant at 0.2 in all simulations, whereas the absolute permeability ( $\mathbf{K}$ ) varied in space, *i.e.*,  $\mathbf{K} = \mathbf{K}(x_i)$ . Fluids are assumed incompressible and gravity was neglected. The set-up for the numerical simulations are summarised in Table 1.

#### 4.2. Initial Model Validation

Numerical simulations (based on lab experiments due to Evans and Dawe, 1994; Dawe and Grattoni, 2008) were conducted to demonstrate the model capability to capture viscous crossflow in immiscible displacement in heterogeneous porous media. The 2D domain, shown in Fig. 4, is 4 × 2 unit-length and fully saturated with fluid 2 ( $VR=1$ ). Fluid 1 is injected from the left-hand side of the domain with constant velocity of  $u = 1$ . Boundary conditions also include no-flux across upper and lower borders. The domain consists of four regions in which each quarter is represented by a permeability value, Fig. 4(a). The spatial discontinuities of permeability distribution will create a rough pressure field, *i.e.*, the pressure gradient is discontinuous across the interface between different permeability zones thus the flow will be led to the high permeability region. This will cause difficulties for numerically solving fluid flows in heterogeneous porous media.

Numerical simulation was performed in modified conditions (see Fig. 4) to assess model behaviour under larger  $VR=10$ . Initial and boundary conditions remain the same, and flow behaviour qualitatively agree validated against laboratory experiments conducted by Evans and Dawe (1994). Figures 4(b) and (c) show the continuous displacement of fluid 2 due to the injection of fluid 1. They also show the development of wetting phase through the four subdomains, demonstrating the preferential flow path through high-permeability regions. Such flow behaviour, represented by the crossflow

through the four regions, is a good qualitative agreement with experiments conducted by [Dawe and Grattoni \(2008\)](#).

#### *4.3. Flow simulations in Hele-Shaw cells at different Viscosity Ratio conditions*

In order to investigate the impact of viscosity ratio on the flow dynamics, numerical simulations of fluid displacement were conducted in Hele-shaw cells (*i.e.*, parallel flat plates separated by infinitesimal space) following the work by [Saffman \(1986\)](#). In this manuscript, the onset of viscous flow instabilities (following his seminal work in [Saffman and Taylor, 1958](#)) is investigated along with the impact of boundary conditions in the problem's mathematical formulation and solutions.

Here, 2D simulations were conducted in a  $5 \times 5$  cm domain (Fig. 5a) fully saturated with a fluid, *i.e.*, *in situ* hydrocarbons. Wetting phase fluid is driven from the bottom left-hand corner of the domain with velocity of  $1 \text{ cm.s}^{-1}$  (magnitude). Newmann (*i.e.*, no flux) boundary conditions were imposed to all borders of the domain except at the top right-hand corner (named as sink), and a pressure gradient between source and sink regions was initially prescribed to the system.

Figures 5-7 show fluid displacement in simulations conducted with  $VR = \{3, 10, 150\}$ , respectively. At relatively low viscosity ratio conditions (*i.e.*,  $VR=3$ ), saturation evolves in time with a smooth front throughout most of the domain, and no finger could be observed. Elongated saturation profile at later stages of the simulation is due to pressure gradient near the sink region. However, formation of fingers can be readily noticed at early stages of the simulation conducted with  $VR=10$ .

Viscous finger morphologies were investigated by [Guan and Pitchumani \(2003\)](#) based on mathematical formulation and semi-analytic solutions of the coupled Darcy and continuity equations developed by [McLean and Saffman \(1981\)](#). A sensitivity study was conducted to assess the impact on fingers' formation, dimensions and branchiness for a range of viscosity ratio ( $10^2 \leq VR \leq 10^4$ ) and modified capillary number ( $632 \leq N'_C \leq 6.32 \times 10^7$ , with  $N'_C = U_f \mu \gamma^{-1} (W/b)^2$ , where  $U_f$  is the velocity of the finger,  $W$  is half Hele-Shaw cell width and  $b$  is the cell thickness). Finger width ( $\lambda_f$ ) and volumetric flow rate ( $Q$ ) at the outflow region are correlated through ([Guan and Pitchumani,](#)

2003),

$$\mathcal{Q} = U_f b \lambda_f. \quad (9)$$

Here, numerical simulations performed with viscosity ratio of 10 and 150 indicated maximum fingers width of approximately 0.45-0.70 and 0.50-0.90 cm (Fig. 11 a and b), respectively. This is in close agreement with expected values obtained from Eqn. 9 which indicates maximum finger width ranging from 0.13 to 0.75 (for  $VR=10$ ) and from 0.30 to 0.75 (depending on finger's tip velocity, Table 2).

Fluid flow dynamics through heterogeneous porous media are sensibly more complex than in homogeneous media and strongly depend on problem properties. Spatial variation in geological formations occurs in all length-scales, where heterogeneity characteristics in small length-scales (*i.e.*, pore) are statistically embedded into permeability (absolute and relative) and porosity parameters. Such multi-scale heterogeneity induces preferential flow pathways and plays a significant role in the onset of fluid instabilities as it triggers fingers formation and their accelerated growth (see Wing et al., 1989; Tchelepi and Jr, 1994).

In order to qualitatively investigate the impact of heterogeneity (here represented by changing in the permeability field), numerical simulations were conducted using a prescribed permeability distribution and viscosity ratios of 10 and 150. Absolute permeability ranging from  $1.0 \times 10^{-12}$  to  $5.0 \times 10^{-10}$   $\text{cm}^2$  (*i.e.*,  $0.1 \leq \mathbf{K} \leq 50$  millidarcy) was used in the simulations, which were performed with the same geometry, mesh resolution, boundary and initial conditions as in previous homogeneous cases.

Figures 8 and 9 show formation of multi-scale elongations with continuous growth and coalescence of dendritic finger branching in simulations performed with viscosity ratio of 10 and 150, respectively. In both simulations, maximum fingers width of approximately 0.44-0.56 ( $VR=10$ ) and 0.24-0.44 cm were found, whereas estimated values (based on Eqn. 9) were 0.25-4.50 ( $VR=10$ ) and 0.88-3.00 cm (Fig. 11 c and d, Table 2). Such calculated ranges (*i.e.*, theoretical values based on analytic solutions due to McLean and Saffman, 1981) clearly overestimate fingers dimensions as the mathematical formulation (and therefore Eqn. 9) assumes incompressible flows in homogeneous porous medium, *i.e.*, it does not take into account any spatial variability of heterogeneity.

#### 4.4. Capturing Flow Dynamics and Fingering Growth: Impact of Mesh Resolution

In most numerical simulations involving geofluid dynamics local geometric constraints (*e.g.*, faults, fractures etc) and spatial multi-scale variability of flow properties are often ignored as the underlying computational mesh grid is too coarse to reliably represent any of these features. Whilst structured grids often struggle to conform to complex domain boundaries with consistent mesh connectivity, unstructured mesh techniques often relax cells' neighbourhood relationship constraints by dividing the domain into polytopes in which elements share adjacent faces. This leads to mesh grids that conform to the domain topography and can make the best use of state-of-the-art self-adaptive computational methods.

In Section 4.3, the impact of viscosity ratio on the growth of fingers and the triggering effect of heterogeneity on instability's nucleation were demonstrated in modified simulated Hele-Shaw cells. In order to capture the continuous development of viscous instabilities, mesh grids with sufficient resolution need to be applied over the interface between fluids. Figure 10 shows a numerical simulation performed with the same geometry, boundary and initial conditions as the one shown in Fig. 9, but with noticeable lower resolution (1768 instead of 26313 P<sub>1</sub>DG-P<sub>2</sub> element-pairs). As can be seen, the lower the resolution the more difficult is to capture the fingers formations.

Traditional numerical methods often rely on fixed git add manuscript mesh with sufficient resolution throughout the domain to capture specific flow dynamics (*e.g.*, fluid instabilities, flow recirculation, heat and mass transfers etc), however computational resources may make it prohibitive for complex geometries and highly heterogeneous properties. Mesh adaptivity methods have been extensively used by the computational geofluid dynamic community to help capturing detailed flow dynamics, compositional non-equilibrium fluid displacement and solid-fluid interactions (Paluszny et al., 2007; Pietro et al., 2014; Su et al., 2016; Melnikova et al., 2016). In these methods, the mesh grid is continuously modified (*i.e.*, adjustments of the number and distribution of the degrees of freedom to reduce solution error) to focus resolution where is necessary as the simulation evolves in time and space. There are four main families of mesh adaptivity methods: adaptive mesh refinement (AMR), edge and face element manipulations whereas keeping the order of the element basis function fixed (h-adaptivity), mesh deformation (r-adaptivity) and changes of element basis function order (p-adaptivity).

Detailed description and analysis of mesh adaptivity methods are beyond the scope of this manuscript but can be readily found in [Lo \(2015\)](#) (see also [Plewa et al., 2004](#); [Frey and George, 2008](#)).

The dynamic mesh adaptive algorithm embedded in the Fluidity/IC-FERST model utilises a metric tensor field dependent on solution interpolation error-estimates which locally control the topology of elements in the metric ([Pain et al., 2001](#); [Power et al., 2006](#)). Mesh optimisation generates unstructured finer mesh in regions where flow properties change faster and coarser mesh in regions where properties change more slowly ([Piggott et al., 2006](#)). The mesh adapts in three stages: metric formation, mesh optimisation and fields' interpolation from the pre- to post-adapted mesh (see [Hiester et al., 2014](#)). In the simulations shown in this work, mesh will adapt as a response to oscillations in the phase saturation field with prescribed interpolation error estimate ([Mostaghimi et al., 2016](#)).

Here, two numerical simulations were conducted with fixed and adaptive mesh resolutions to qualitatively assess model capability to capture fingers dynamics. In order to trigger the formation of fingers, regions with sharp permeability gradient were introduced. The computational space, Fig. 12a, consists of a rectangular domain fully saturated with a fluid (except by a squared region containing 50% of a second fluid – wetting fluid phase, Fig. 12b) and divided into 5 regions with prescribed permeability distribution. A no-flux boundary condition was imposed on upper and lower borders, whilst pure wetting fluid phase (*i.e.*,  $S_1 = 1$ ) is driven into the domain from the left-hand face at velocity  $u_1 = 1$ . Viscosity ratio was set to 10.

Figures 13 and 14 show fluid displacement in simulations performed with fixed and adaptive meshes. Both simulations started with a mesh of 13068 triangular ( $P_1$ DG- $P_2$ ) elements, however as flow dynamics evolve the number of elements of the simulation conducted with adaptive mesh oscillates from a minimum of 4400 to a maximum of 16430 (Fig. 15). In both cases, fingers' development (formation, growth and coalescence) and fluid cross flows (through regions of distinct permeabilities at the top of the domain,  $\mathbf{K} = \{2, 3\}$ ) can be readily noticed. The simulation performed with a fixed and relatively fine mesh was able to capture the progressive development of fingers (as shown in Fig. 16b) prompted by sharp permeability gradient at the interface of regions with  $\mathbf{K} = \{1, 5\}$ . In regions with no permeability gradient, formation and development of fingers (Fig. 16c) were not captured by the simulation conducted with fixed mesh. In both cases, dynamic adaptive mesh based

on perturbation of phase saturations with imposed interpolation error estimate proved to be able to capture the onset of instabilities and fingers' development with relatively little computational overhead.

#### 4.5. 3-D channel flows

In this section, 3D simulations are introduced to investigate preferential flow pathways and finger growth through semi-pervious and impervious layers, as described in Figure 17. In large scale geological formations preferential flow may allow fast contaminant transport and creates significant consequences for ground-water quality, and low recovery rate in hydrocarbon production fields.

As mentioned in Section 3, *viscous fingering* is characterized by the formation of flow patterns, called viscous fingers. The geometrical evolution of these patterns provides good indications on capturing and tracking any instabilities in the flow front. Figure 17 shows the initial permeability distribution for the simulations described in this section. The surface on the left hand side of the domain is the area where fluid 1 is injected with a uniform velocity of  $2.5 \text{ cm.s}^{-1}$ . No-slip conditions are applied everywhere else (*i.e.*, no flux across the boundaries) except at the right hand side of the domain where the fluid is allowed to leave the domain. Initially, the domain was partially saturated with non-wetting fluid, *i.e.*,  $S_{nw}(t = 0) = 0.80$ , which was displaced by a pure (wetting) fluid. The domain was designed to capture preferential flow pathways, as shown in Fig. 18-20.

Flow pathways are clearly indicated in Fig. 18, where fluid 1 Darcy velocity vectors overlapped with fluid saturation are shown. Fluid displacement occurs mainly in regions of relatively larger permeability, leaving other parts of the domain (*i.e.*, regions with low permeability distribution) with little or no momentum, indicating that at these regions the non-wetting fluid (*i.e.*, fluid 2) are not effectively displaced.

In Sections 4.1-4.4, a 2D domain was used to describe one or more finger formations. These flow instabilities were triggered from the permeability differences in the domain. Using a 3D domain, the difference between a flow instability and the preferential flow path that may include smaller fingers is more obvious as the latter may include finger formations. Figure 19 describes the flow path in various instances of time showing the progression of the saturation front that now becomes more distinct. Heterogeneity is determine

by the spatial distribution of porosity ( $\phi = 0.20$  in the current case) and permeability.

The progress of the saturation front and formation and growth of fingers in time and space can be seen in more details in isosurfaces shown in Fig. 20. However due to relatively low mesh resolution, in particular above and below the central channel region, capture of fingers (formation and growth) was very limited. In figures 21(a)-(f) an unstructured and adaptive mesh has been introduced in order to achieve higher resolution and focus the computational effort where is needed in the domain. For the same time-steps an inner view on the domain provides with a more detailed description of not only the flow path itself as well as the minor fingers that may be created. At this point resolution plays an important role on capturing these patterns in detail and is also a limitation that needs to be overcome.

A quick review to the mechanisms of viscous fingering (*i.e.*, shielding, spreading and tip-splitting, [Homsy \(1987\)](#)) is required. In all the 2D previous cases (sections 4.1-4.4), as interfacial surface tension (IFT) becomes weak, the front of the steady finger is susceptible to a viscous-fingering instability. Through *shielding* mechanism, one of these fingers will eventually outgrow the other and, will then spread (*spreading*) to occupy the appropriate width of the domain ahead of it. Following this process, it reaches a width that is again unstable and the pattern repeats. So far shielding and spreading were dominating the flow but, using the current 3D domain and by applying two types of meshes, despite the resolution restrictions, the conditions and the mechanics of tip-splitting along a front can be qualitatively understood.

## 5. Conclusions

A number of different cases have been illustrated in Section 4. Starting from testing experimental cases and geometrical domains (Hele-shaw domain) to verify that the numerical model is working and set up some initial benchmarks, to more complicated cases where various scenarios were implied. Observations made on various mobility ratios, geometrical domains and permeability zones as well as on the role of interfacial forces and fingering mechanisms on the development of the flows.

For immiscible displacements upon which only viscous and capillary forces are acting, the expected displacement patterns are either fully developed

cross flow displacement or unstable front displacement. In the latter case the instability rises due to viscous fingering depending on capillary number ( $N_c$ ) but mainly is a function of viscosity ratio (*i.e.*, VR). If the mobility ratio is significantly less than 5, it is expected to find capillary fingering at relatively low flow rate and viscous fingering at relatively high flow rate. On the other hand, when the viscosity ratio is greater than 5, the two basic forms of immiscible displacement are capillary fingering at relatively low flow rate and stable displacement at relatively high flow rate. Therefore for an *i.e.*, water/oil system, the first condition applies as the viscosity of injected water is less than the viscosity of displaced oil. Hence, the displacement front could be either capillary fingering at relatively low injection rates or viscous fingering at higher injection rates.

As seen for high viscosity contrast, there is a leading finger (*tip splitting mechanism*) that breaks out of the front by suppressing its growth to the point that smaller fingers will break out driven by surface tension. At long times the large finger advances approximately at a constant flow rate. In order to run all these simulations in detail, the use and benefits of dynamic mesh adaptivity to capture the viscous fingering in reservoir flows was introduced for all the 2D and 3D cases. Commercial simulators provide the user with option of an unstructured type of mesh, still they are not able to dynamically adapt the mesh where is needed and manage the computational cost more efficient.

In summary, the method that has been described in this paper as well as the simulations performed have a number of distinct advantages:

1. The geological model can be designed from the beginning without any previous reference or geometrical limitations due to both the flexibility of method and to the fact that the geological characteristic and parameters can be easily introduced.
2. Computational cost can be reduced, because the complex geometries and surfaces are less expensive to generate and manage using fewer grid cells. The basis of this argument is the flexibility and variance of the adaptive and unstructured grid in time and space.
3. Production simulations run directly on the geological model without the need to upscale.

Regarding the flow characteristics and the mechanics of fingering formations,

1. After having separate the cross flow pattern from the viscous finger one, the findings show that the displacing fluid tends to flow easier towards the zones with higher values of permeability, as these can be seen from evolution of fingers in the upper layers of the domains or from longitudinal section throughout the Hele-shaw domains.
2. Even though different permeability patterns will initially make the uniform front to collapse, it is the *viscosity ratio* the key parameter and the capillary forces as these are related with surface tension that will eventually lead the flow instabilities. The higher the viscosity ratio the easier it is for the uniform front of the injected fluid to break into fingers that eventually will decrease the recovery of hydrocarbon content.
3. The increased viscosity ratio increases the computational cost and requires the use of smaller time-step sizes.
4. Properties such as porosity and saturation can be readily up-scaled as they can be included in the element boundaries. The domains used in these test-cases have the ability to describe the fingering mechanism and the development of the flow *i.e.*, the latter case clearly describes the linear tip-splitting finger behaviour inside the domain.

## 6. Acknowledgements

Mr William Radünz would like to acknowledge the support from the Brazilian Research Council (CNPq) under the *Science without Borders scholarship programme*. Mr Konstantinos Christou would like to acknowledge the support of the University of Aberdeen - College of Physical Science as well as the Aberdeen Formation Evaluation Society (*AFES* is an SPWLA chapter).

## References

- Adam, A., Pavlidis, D., Percival, J., Salinas, P., Xie, Z., Fang, F., Muggeridge, A., Jackson, M., 2016. Higher-order conservative interpolation between control-volume meshes: Application to advection and multiphase flow problems with dynamic mesh adaptivity. *Journal of Computational Physics* 321, 512–531.
- Adler, P. M., Brenner, H., 1988. Multiphase flow in porous media. *Ann. Rev. Fluid Mechanics* 20, 35–59.
- Alpak, F., Lake, L., Embid, S., 1999. Validation of a modified carman-kozeny equation to model two-phase relative permeabilities. In: SPE Annual Technical Conference and Exhibition. SPE, Texas, SPE56479.
- AMCG, July 2010. A User's Guide for the Fluidity Model. Applied Modelling and Computation Group – AMCG.
- AMCG, April 2012. POROSITY: A new state-of-art unstructured adaptive-mesh reservoir model – developers' documentation. Tech. rep., internal Communication.
- Aziz, K., Settari, A., 1986. Fundamentals of reservoir simulation. Elsevier Applied Science Publishers, New York.
- Bottino, M., Sengpiel, W., 1992. Review of mathematical and physical basis of two-phase flow modeling. NASA STI / Recon Technical Report 94.
- Brooks, R., Corey, A., 1964. Hydrology Papers. Vol. 3. Colorado State University, Ch. Hydraulic properties of porous media.
- Chang, Y., Pope, G., K.Seperhnoori, 1990. A higher-order finite difference compositional simulator. *Journal of Petroleum Science and Engineering* 5, 35–50.
- Chavent, G., Jaffré, J., 1986. Mathematical Models and Finite Elements for Reservoir Simulation. Vol. 17 of Studies in Mathematics and Its Applications. North Holland.
- Chen, Z., Huan, G., Ma, Y., 2006. Computational Methods for Multiphase Flows in Porous Media. SIAM.

- Chen, Z., Huan, G., Wang, H., 2005. Simulation of a compositional model for multiphase flow in porous media. *Numerical Methods for Partial Differential Equations* 21 (4), 726–741.
- Cotter, C., Ham, D., C.C, P., Reich, S., 2009. LBB stability of a mixed discontinuous/continuous galerkin finite element pair. *Journal of Computational Physics* 228, 336–348.
- Courant, R., Friedrichs, K., Lewy, H., 1941. On difference equations of mathematical physics. *Uspekhi Mat. Nauk* 8, 125–160.
- Cumming, B., 2012. Modelling sea water intrusion in coastal aquifers using heterogeneous computing. Ph.D. thesis, Queensland University of Technology, Australia.
- Cumming, B., Moroney, T., Turner, I., 2011. A mass-conservative control volume-finite element method for solving Richards' equation in heterogeneous porous media. *BIT Numerical Mathematics* 51 (4), 845–864.
- Dawe, R., Grattoni, C., 2008. Experimental displacement patterns in a  $2 \times 3$  quadrant block with permeability and wettability heterogeneities problems for numerical modelling. *Transport in Porous Media* 71, 5–22.
- Evans, R., Dawe, R., 1994. The danger of neglecting nodal crossflow in heterogeneous near-wellbore conditions. *Journal of Petroleum Science and Engineering* 11 (2), 113–121.
- Frey, P., George, P.-L., 2008. Mesh Generation, 2nd Edition. Wiley.
- Fung, L., Hiebert, A., Nghiem, L., 1992. Reservoir simulation with control-volume finite element method. *SPE Reservoir Engineering* 7 (3), 349–357.
- Gomes, J., Pavlidis, D., Salinas, P., Percival, J., Xie, Z., Melnikova, Y., Pain, C., Jackson, M., 2017. A force balanced control volume finite element method for multi-phase porous media flow modelling. *Int. J. Numer. Methods in Fluids* 83, 431–455.
- Gomes, J., Tollit, B., Milles, B., Pain, C., 2012. Fluidization Engineering – Principles and Practice. National University of Singapore, Singapore, Ch. Multi-Physics Flow Modelling for Nuclear Applications.

- Guan, X., Pitchumani, R., 2003. Viscous fingering in a hele-shaw cell with finite viscosity ratio and interfacial tension. *Transactions of the ASME* 125, 354–364.
- Habermann, B., 1960. The efficiency of miscible displacements as a function of mobility ratio. *Petroleum Transactions, AIME* 219, 264–272.
- Hiester, H., Piggott, M., Farrell, P., Allison, P., 2014. Assessment of spurious mixing in adaptive mesh simulations of the two-dimensional lock exchange. *Ocean Modelling* 73, 30–44.
- Homsy, G., 1987. Viscous fingering in porous media. *Ann. Rev. Fluid Mechanics* 19, 271–311.
- Howison, S. D., 2000. A note on the two-phase hele-shaw problem. *Journal of Fluid Mechanics* 409, 243–249.
- Jackson, M., Gomes, J., Mostaghimi, P., Percival, J., Tollit, B., Pavlidis, D., Pain, C., El-Sheikh, A., Muggeridge, A., Blunt, M., 2013. Reservoir modeling for flow simulation using surfaces, adaptive unstructured meshes, and control-volume-finite-element methods. In: *SPE Reservoir Simulation Symposium*.
- Jackson, M., Percival, J., Mostaghimi, P., Tollit, B., Pavlidis, D., Pain, C., Gomes, J., ElSheikh, A., Salinas, P., Muggeridge, A., Blunt, M., 2014. Reservoir modeling for flow simulation by use of surfaces, adaptive unstructured meshes, and an overlapping-control-volume finite-element method. *SPE Reservoir Evaluation & Engineering* 18 (2), SPE-163633-PA.
- Jiang, X., 2011. A review of physical modelling and numerical simulation of long-term geological storage of carbon dioxide. *Applied Energy* 88, 3557–3566.
- King, M., Mansfield, M., 1999. Flow simulation of geologic models. *SPE Reservoir Evaluation & Engineering* SPE-57469-PA.
- Kirkland, M., Hills, R., Wierenga, P., 1992. Algorithms for solving Richards' equation for variably-saturated soils. *Water Resources Research* 28, 2049–2058.
- Lo, S., 2015. *Finite Element Mesh Generation*. CRC Press.

- Lux, J., Anguy, Y., 2012. A study of the behavior of implicit pressure explicit saturation (IMPES) schedules for two-phase flow in dynamic pore network models. *Transp. Porous Med.* 93, 203–221.
- McLean, J., Saffman, P., 1981. The effect of surface tension on the shape of fingers in a hele-shaw cell. *J. Fluid Mechanics* 102, 455–469.
- Melnikova, Y., Jacquemyn, C., Osman, H., Salinas, P., Gorman, G., Hampson, G., Jackson, M., 2016. Reservoir modelling using parametric surfaces and dynamically adaptive fully unstructured grids. In: Proceedings of the XV European Conference on the Mathematics of Oil Recovery (ECMOR XV). EAGE.
- Mlacnik, M., Durlofsky, L., Heinemann, Z., 2004. Dynamic flow-based PEBI grids for reservoir simulation. SPE 90009.
- Mostaghimi, P., Kamall, F., Jackson, M., Muggeridge, A., Pain, C., 2016. Adaptive mesh optimisation for simulation of immiscible viscous fingering. *SPE Journal* 21, 250–259.
- Muskat, M., 1934. Two fluid systems in porous media. the encroachment of water into an oil sand. *Journal of Applied Physics* 5, 250–264.
- Nick, H., Matthai, S., 2011a. Comparison of three fe-fv numerical schemes for single- and tw-phase flow simulation of fractured porous media. *Transp. Porous Med* 90, 421–444.
- Nick, H., Matthai, S., 2011b. A hybrid finite-element finite-volume method with embedded discontinuities for solute transport in heterogeneous media. *Vadose Zone Journal* 10, 299–312.
- Pain, C., Umpleby, A., de Oliveira, C., Goddard, A., 2001. Tetrahedral mesh optimisation and adaptivity for steady-state and transient finite element calculations. *Computer Methods in Applied Mechanics and Engineering* 190, 3771–3796.
- Paluszny, A., Matthai, S., Hohmeyer, M., 2007. Hybrid finite element finite colume discretization of complex geologic structures and a new simulation workflow demonstrated on fractured rocks. *Geofluids* 7, 186–208.

- Pavlidis, D., Gomes, J., Xie, Z., Percival, J., Pain, C., Matar, O., 2016. Compressive advection and multi-component methods for interface-capturing. International Journal for Numerical Methods in Fluids 80 (4), 256–282.
- Pietro, D. D., Vohralík, M., Yousef, S., 2014. An a posteriori-based, fully adaptive algorithm with adaptive stopping criteria and mesh refinement for thermal multiphase compositional flows in porous media. Computers and Mathematics with Applications 68 (12B), 2331–2347.
- Piggott, M., Pain, C., Gorman, G., Power, P., Goddard, A., 2006. h,r and hr adaptivity with application in numerical ocean modelling. Ocean Modelling 10, 95–113.
- Plewa, T., Linde, T., Weirs, V. (Eds.), 2004. Adaptive Mesh Refinement – Theory and Applications. Vol. 41 of Lecture Notes in Computational Science and Engineering. Springer.
- Power, P., Piggott, M., Fang, F., Gorman, G., Pain, C., Marshall, D., Goddard, A., 2006. Adjoint goal-based error norms for adaptive mesh ocean modelling. Ocean Modelling 15, 3–38.
- Praud, O., Swinney, H. L., Jul 2005. Fractal dimension and unscreened angles measured for radial viscous fingering. Phys. Rev. E 72, 011406.
- Radünz, W., Oliveira, F., Gomes, J., July 2014. A multi-scale model of multi-fluid flows transport in dual saturated-unsaturated heterogeneous porous media. In: Onate, E., Oliver, J., Huerta, A. (Eds.), Proceedings of the XI World Congress on Computational Mechanics (WCCM XI). IACM/ECCOMAS, Barcelona, Spain.
- Riaz, A., Tchelepi, H. A., 2004. Linear stability analysis of immiscible two-phase flow in porous media with capillary dispersion and density variation. Physics of Fluids 16 (12), 4727–4737.
- Saffman, P., 1959. Theory of dispersion in porous medium. J. Fluid Mechanics 6, 321–349.
- Saffman, P., 1986. Viscous fingering in hele-shaw cells. J. Fluid Mechanics 173, 73–94.

- Saffman, P., Taylor, G. I., 1958. The penetration of a fluid into a porous medium or hele-shaw cell containing a more viscous liquid. Proc. R. Soc. London A 245, 321–329.
- Salinas, P., Percival, J., Pavlidis, D., Xie, Z., Gomes, J., Pain, C., Jackson, M., et al., 2015. A discontinuous overlapping control volume finite element method for multi-phase porous media flow using dynamic unstructured mesh optimization. In: SPE-173279-MS, Reservoir Simulation Symposium. Society of Petroleum Engineers.
- Self, S., Reddy, B., Rosen, M., 2012. Review of underground coal gasification technologies and carbon capture. International Journal of Energy and Environmental Engineering 3, 16–24.
- Spycher, N., Pruess, K., Ennis-King, J., 2003. CO<sub>2</sub>-H<sub>2</sub>O mixtures in the geological sequestration of CO<sub>2</sub>. II. Assessment and calculation of mutual solubilities from 12 to 100°C and up to 600 bar. Geochim. Cosmochim. Acta 67 (16), 2015–3031.
- Su, K., Latham, J., Pavlidis, D., Xiang, J., Fang, F., Mostaghimi, P., Percival, J., Pain, C., Jackson, M., 2016. Multiphase flow simulation through porous media with explicitly resolved fractures. Geofluids 15, 592–607.
- Tabeling, P., Zocchi, G., Libchaber, A., 1987. An experimental study of the saffman-taylor instability. Journal of Fluid Mechanics 177, 6782.
- Tavassoli, S., Pope, G. A., Sepehrnoori, K., et al., 2015. Frontal-stability analysis of surfactant floods. SPE Journal 20 (03), 471–482.
- Tchelepi, H., Jr, F. O., 1994. Interaction of viscous fingering, permeability heterogeneity and gravity segregation in three dimensions. SPE.
- Voller, V., 2009. Basic Control Volume Finite Element Methods for Fluids and Solids. Vol. 1 of IISc Research Monographs Series. World Scientific Publishing Co, Singapore.
- White, I., Lewis, R., W, L, W., 1981. The numerical simulation of multiphase flow through a porous medium and its application to reservoir engineering. Applied Mathematical Modelling 5, 165–172.

Wing, R., Russel, T., Young, L., 1989. An anisotropic coarse-grid dispersion model of heterogeneity and viscous fingering in five-spot miscible displacement that matches experiments and fine-grid simulations. SPE 18441, 447–465.

Wooding, R. A., Morel-Seytoux, 1976. Multiphase fluid flow through porous media. Ann. Rev. Fluid Mechanics 8, 233–2741.

## List of Tables

- |   |  |    |
|---|--|----|
| 1 | Sumary of model set-up used in the numerical simulations.<br>Superscript $\circ$ denotes initial condition. $\mathbf{K}_i$ is in $cm^2$ and $u_w^\circ$ is in m/sec. $S_{w,irr}$ and $S_{nw,r}$ are the same for all simulations.  | 28 |
| 2 | Flow simulations in Heleshaw cells (Section 4.3): summary of finger width calculations using Eqn. 9 and obtained through numerical simualtions. $\lambda_f^{\text{calc}}$ was calculated based on fingers' tip velocities and outflow rate. Calculations were based on simulation data obtained from snapshots shown in Fig. 11. . . | 29 |

<b>Section</b>	$\phi$	VR	$S_w^0$	$S_{nw}^0$	$\mathbf{K}_1$	$\mathbf{K}_2$	$\mathbf{K}_3$	$\mathbf{K}_4$	$S_{w,irr}$	$S_{nw,r}$	$u_w^\circ$
<b>4.2</b>	0.2	1.0	0.0	1.0	2.5	1.0	N/A	N/A	0.2	0.3	1.0
<b>4.3(homogenous)</b>	0.2	10.0	0.0	1.0	1.e-10	N/A	N/A	N/A	0.2	0.3	0.5
<b>4.3(heterogenous)</b>	0.2	1.0	0.0	1.0	1.e-11 – 5.e-10	1.e-12 – 5.e-10	1.e-12 – 1.e-10	1.e-10	0.2	0.3	1.0
<b>4.4</b>	0.2	1.0	0.0	1.0	3.0	2.0	5.0	1.0	0.2	0.3	0.5
<b>4.5</b>	0.2	1.0	0.0	1.0	3.0	2.0	5.0	1.0	0.2	0.3	0.5

Table 1: Sumary of model set-up used in the numerical simulations. Superscript  $\circ$  denotes initial condition.  $\mathbf{K}_i$  is in  $cm^2$  and  $u_w^\circ$  is in m/sec.  $S_{w,irr}$  and  $S_{nw,r}$  are the same for all simulations.

	<b>K</b> (cm <sup>2</sup> )	<i>VR</i>	$\lambda_f^{(\text{calc,max})}$ (cm) (Eqn. 9)	$\lambda_f^{(\text{simul,max})}$ (cm)
<b>Case 1</b> (homogeneous)	$1 \times 10^{-10}$	10	0.13-0.75	0.45-0.70
<b>Case 2</b> (homogeneous)	$1 \times 10^{-10}$	150	0.30-0.75	0.50-0.90
<b>Case 3</b> (heterogeneous)	$1 \times 10^{-12}$ - $5 \times 10^{-10}$	10	0.25-4.50	0.44-0.56
<b>Case 4</b> (heterogeneous)	$1 \times 10^{-12}$ - $5 \times 10^{-10}$	150	0.88-3.00	0.24-0.40

Table 2: Flow simulations in Heleshaw cells (Section 4.3): summary of finger width calculations using Eqn. 9 and obtained through numerical simulations.  $\lambda_f^{\text{calc}}$  was calculated based on fingers' tip velocities and outflow rate. Calculations were based on simulation data obtained from snapshots shown in Fig. 11.

## List of Figures

1	2D representation of P <sub>1</sub> DG-P <sub>2</sub> element pairs used in this work. Shaded areas denote control volumes across two contiguous elements. Blue and white circles represent pressure and velocity nodes, respectively. . . . .	33
2	This is a graphical representation of two different element types. Triangle <i>A</i> is a representation of the P <sub>1</sub> DG-P <sub>2</sub> element-pair, whereas triangle <i>B</i> represents the P <sub>1</sub> DG-P <sub>1</sub> element-pair. Porosity $\phi_i$ , permeability $\mathbf{K}_i$ , velocity and pressure are primarily represented in FE space whereas scalar fields (such as saturation, density, viscosity etc) are represented in CV space. . . . .	34
3	Schematics of formation of flow instabilities during injection of a pure low viscosity fluid (red) into a domain saturated with a second fluid (dark blue). The viscosity ratio of the two fluids is VR=5. In this case, the initially piston shape front collapses leading to the formation of several fingers. . . . .	35
4	Model validation of fluid displacement in heterogeneous porous media (VR=1): (a) the domain is divided into four subdomains with prescribed synthetic permeability, $K_1 = 1$ and $K_2 = 2.5$ ; (b-c) snapshots of saturation (displacing fluid) field at t=25s and t=300 sec. The domain is discretised with 5960 P <sub>1</sub> DG-P <sub>2</sub> elements. . . . .	36
5	Simulated flow in a Hele-Shaw cell (VR=3, $K=10^{-10}\text{cm}^2$ ): (a) initial pressure profile (in $\text{g.cm}^{-1}.\text{s}^{-2}$ ) with source and sink regions are explicitly shown along with dimensions (in cm); (b-f) snapshots of wetting phase saturation showing flow profile as the simulation evolves. The domain contains 26313 P <sub>1</sub> DG-P <sub>2</sub> triangular elements. . . . .	37
6	Simulated flow in a Hele-Shaw cell (VR=10, $K=10^{-10}\text{cm}^2$ ): snapshots of overlapped wetting phase saturation and velocity vectors showing flow profile as the simulation evolves. The domain contains 26313 P <sub>1</sub> DG-P <sub>2</sub> triangular elements. . . . .	38
7	Simulated flow in a Hele-Shaw cell (VR=150, $K=10^{-10}\text{cm}^2$ ): snapshots of wetting phase saturation showing flow profile as the simulation evolves. The domain contains 26313 P <sub>1</sub> DG-P <sub>2</sub> triangular elements. . . . .	39

8	Simulated flow in a modified Hele-Shaw cell with $VR=10$ : (a) permeability distribution ( $10^{-10} \leq \mathbf{K}_1 \leq 5 \times 10^{-10}$ , $\mathbf{K}_2=10^{-10}$ , $10^{-11} \leq \mathbf{K}_3 \leq 5 \times 10^{-10}$ and $10^{-12} \leq \mathbf{K}_4 \leq 5 \times 10^{-10} \text{ cm}^2$ ); (b-f) snapshots of saturation profile during 9.77 seconds of simulation. The domain contains 26313 P <sub>1</sub> DG-P <sub>2</sub> element-pairs.	40
9	Simulated flow in a modified Hele-Shaw cell with $VR=150$ : snapshots of saturation profile during 2.50 seconds of simulation. Permeability distribution used in this simulation was the same as shown in Fig. 8a. The domain contains 26313 P <sub>1</sub> DG-P <sub>2</sub> element-pairs.	41
10	Simulated flow in a modified Hele-Shaw cell with $VR=150$ : snapshots of saturation profile. Permeability distribution used in this simulation was the same as shown in Fig. 8a. The domain contains 3734 P <sub>1</sub> DG-P <sub>2</sub> element-pairs.	42
11	Isosurfaces of simulated flows in Hele-Shaw cells with viscosity ratios of 10 (a and c) and 150 (b and d). Top and bottom rows describe simulations performed with constant <i>i.e. homogeneous</i> with $\mathbf{K}=10^{-10} \text{ cm}^2$ and randomly distributed (i.e. heterogeneous, Fig. 8a) permeabilities. Width of largest fingers for homogeneous cases are approximately 0.70 and 0.90cm ( $VR=10$ and $VR=150$ , respectively), whereas for heterogeneous cases are 0.56 and 0.40cm. Results for homogeneous cases are in good agreement with values obtained from Guan and Pitchumani (2003)'s analytic solution.	43
12	Impact of mesh resolution on capturing flow instabilities: (a) permeability and (b) initial saturation and mesh resolution used in the simulations performed in Section 4.4. There are 13068 P <sub>1</sub> DG-P <sub>2</sub> element-pairs in the domain.	44
13	Impact of mesh resolution on capturing flow instabilities: snapshots of saturation field through 1.50 seconds of numerical simulation performed with fixed mesh (of 13068 elements) and $VR=10$ .	45
14	Impact of mesh resolution on capturing flow instabilities: snapshots of saturation field through 1.50 seconds of numerical simulation performed with adaptive mesh and $VR=10$ .	46
15	Impact of mesh resolution on capturing flow instabilities: total number of elements and nodes for simulations performed with fixed and adaptive mesh.	47

16	Impact of mesh resolution on flow instabilities: capturing formation and growth of flow instabilities at fluid interfaces ( $t = 0.20$ s) in two regions of the computational domain, $A$ and $B$ . Simulations were conducted with fixed (left-hand side) and adaptive meshes. . . . .	48
17	3D channel flow: permeability distribution. The domain contains 243056 $P_1$ DG- $P_1$ element-pairs. . . . .	49
18	3D channel flow: XY and YZ planes showing wetting fluid phase Darcy velocity vectors overlapped with wetting fluid saturation at (a) $t=0.29$ s and (b) $t=4.3$ s. . . . .	50
19	3D channel flow: saturation front evolving in time and space with preferential flow pathways through 3.50 seconds of numerical simulations. Preferential flow pathway can be readily noticed in these frames, mirroring permeability distribution. The domain contains 368513 $P_1$ DG- $P_1$ elements. . . . .	51
20	3D channel flow: Isosurfaces for wetted phase saturation ranging from 0.45 and 0.60 at the same instants of time of Fig. 19. Preferential flow pathway can be readily noticed in (b) and (f). Fingers' formation and growth can be clearly noticed in (b)-(e). The domain contains 368513 $P_1$ DG- $P_1$ elements. . . . .	52
21	For the same time steps as these are shown in figure 19 there is a description of the same flow path but now using an adaptive and unstructured mesh. The aim was to describe in greater detail the finger patterns, as the flow develops but also address the importance of a resolution, in this case the type of mesh that is used to capture these phenomena. . . . .	53
22	This is a qualitative comparison at $t=\text{end}$ of simulation, for bot the fixed and unstructured mesh used in the 3D domain. . . . .	54
23	3D Channel: Text to come . . . . .	55
24	3D Channel: Text to come should i mention something here? . . . . .	56

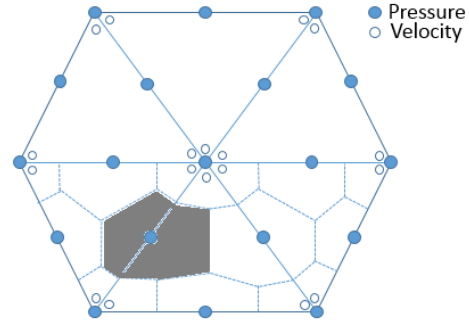


Figure 1: 2D representation of  $P_1$ DG- $P_2$  element pairs used in this work. Shaded areas denote control volumes across two contiguous elements. Blue and white circles represent pressure and velocity nodes, respectively.

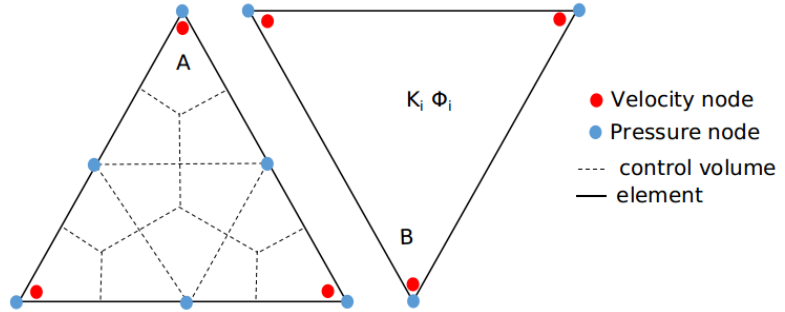


Figure 2: This is a graphical representation of two different element types. Triangle *A* is a representation of the P<sub>1</sub>DG-P<sub>2</sub> element-pair, whereas triangle *B* represents the P<sub>1</sub>DG-P<sub>1</sub> element-pair. Porosity  $\phi_i$ , permeability  $\mathbf{K}_i$ , velocity and pressure are primarily represented in FE space whereas scalar fields (such as saturation, density, viscosity etc) are represented in CV space.

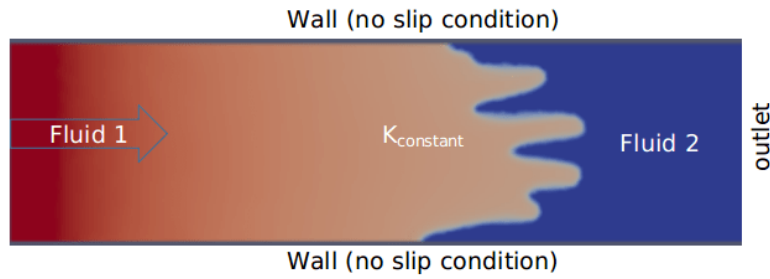
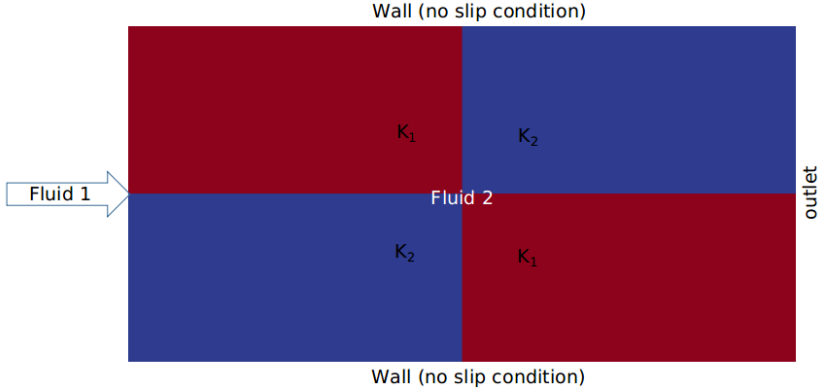
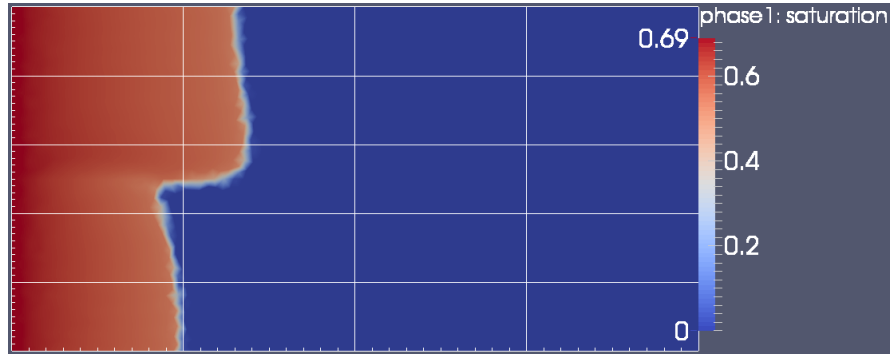


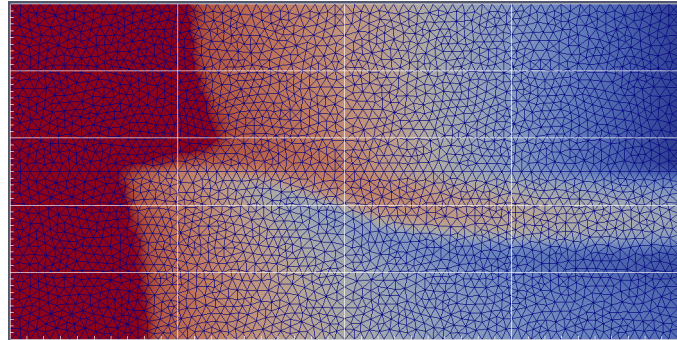
Figure 3: Schematics of formation of flow instabilities during injection of a pure low viscosity fluid (red) into a domain saturated with a second fluid (dark blue). The viscosity ratio of the two fluids is  $VR=5$ . In this case, the initially piston shape front collapses leading to the formation of several fingers.



(a) Schematics of the domain with permeability ( $\mathbf{K}$ ) distribution



(b) flow at  $t=250$



(c) flow at  $t=3000$

Figure 4: Model validation of fluid displacement in heterogeneous porous media ( $VR=1$ ):  
(a) the domain is divided into four subdomains with prescribed synthetic permeability,  
 $\mathbf{K}_1 = 1$  and  $\mathbf{K}_2 = 2.5$ ; (b-c) snapshots of saturation (displacing fluid) field at  $t=25$ s and  
 $t=300$  sec. The domain is discretised with 5960  $P_1$ DG- $P_2$  elements.

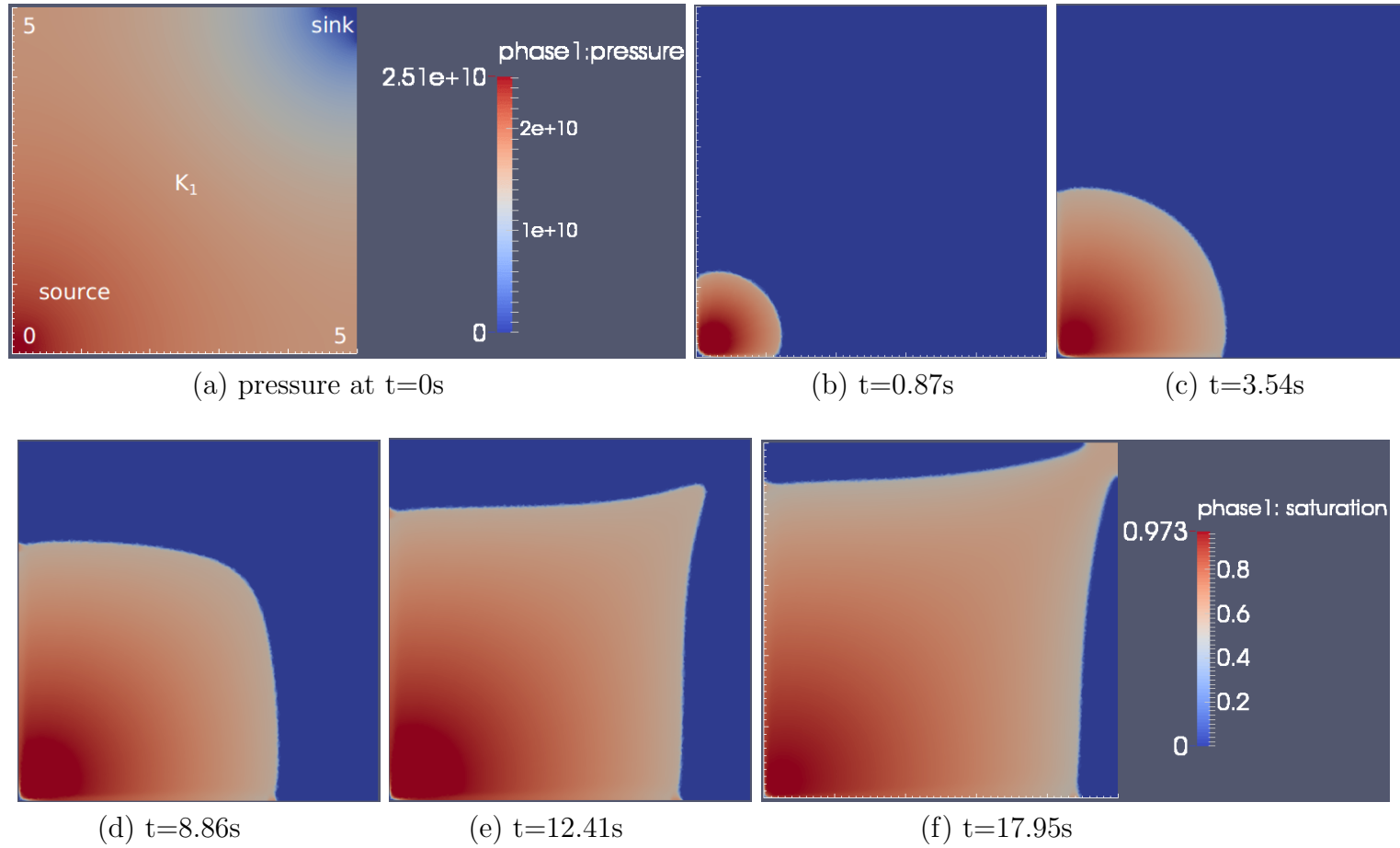


Figure 5: Simulated flow in a Hele-Shaw cell ( $VR=3$ ,  $K=10^{-10}\text{cm}^2$ ): (a) initial pressure profile (in  $\text{g.cm}^{-1}.\text{s}^{-2}$ ) with source and sink regions are explicitly shown along with dimensions (in cm); (b-f) snapshots of wetting phase saturation showing flow profile as the simulation evolves. The domain contains 26313  $P_1$ DG- $P_2$  triangular elements.

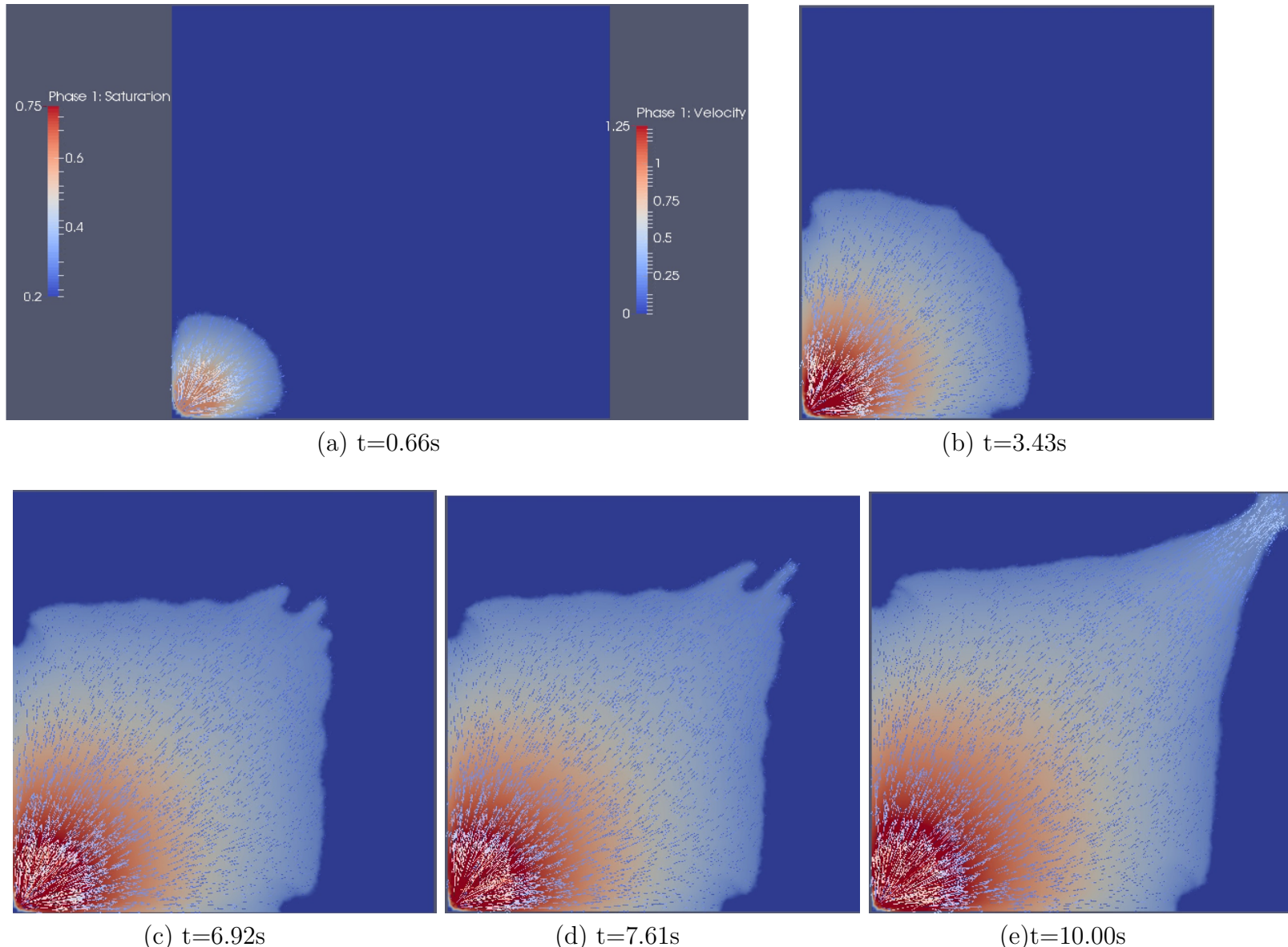


Figure 6: Simulated flow in a Hele-Shaw cell ( $VR=10$ ,  $\mathbf{K}=10^{-10}\text{cm}^2$ ): snapshots of overlapped wetting phase saturation and velocity vectors showing flow profile as the simulation evolves. The domain contains 26313  $P_1$ DG- $P_2$  triangular elements.

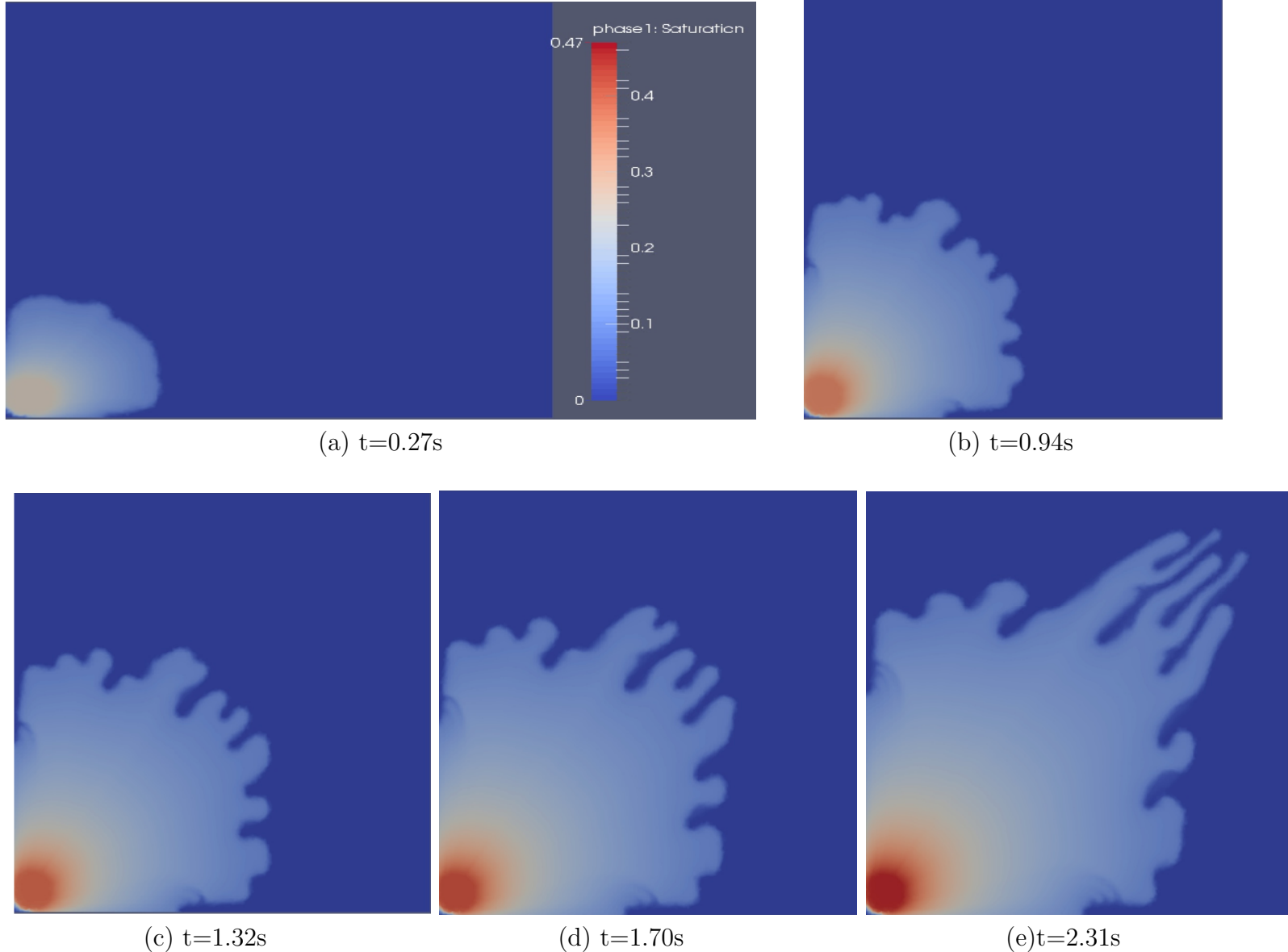


Figure 7: Simulated flow in a Hele-Shaw cell ( $VR=150$ ,  $\mathbf{K}=10^{-10}\text{cm}^2$ ): snapshots of wetting phase saturation showing flow profile as the simulation evolves. The domain contains 26313  $P_1$ DG- $P_2$  triangular elements.

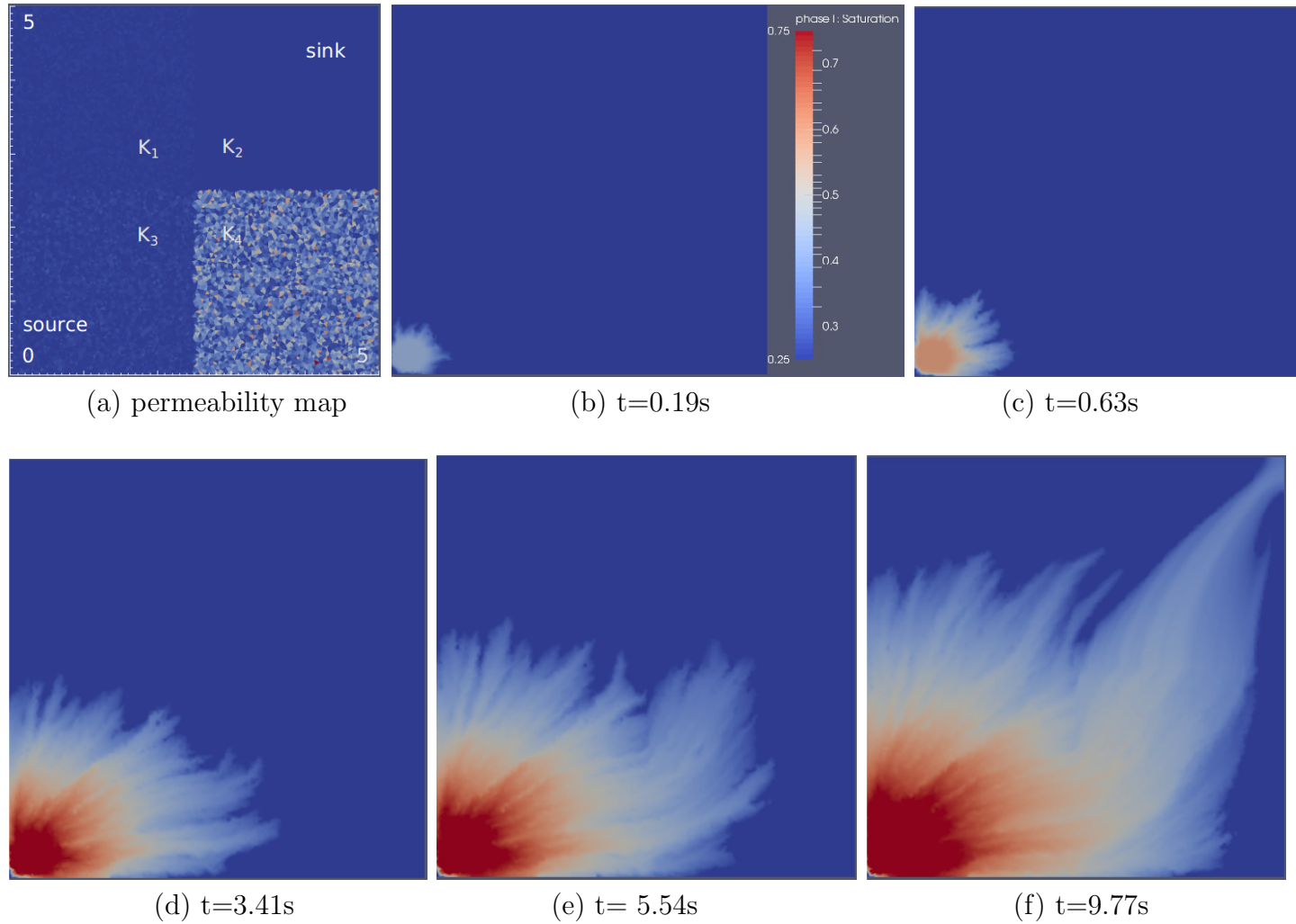


Figure 8: Simulated flow in a modified Hele-Shaw cell with  $VR=10$ : (a) permeability distribution ( $10^{-10} \leq \mathbf{K}_1 \leq 5 \times 10^{-10}$ ,  $\mathbf{K}_2=10^{-10}$ ,  $10^{-11} \leq \mathbf{K}_3 \leq 5 \times 10^{-10}$  and  $10^{-12} \leq \mathbf{K}_4 \leq 5 \times 10^{-10} \text{ cm}^2$ ); (b-f) snapshots of saturation profile during 9.77 seconds of simulation. The domain contains 26313 P<sub>1</sub>DG-P<sub>2</sub> element-pairs.

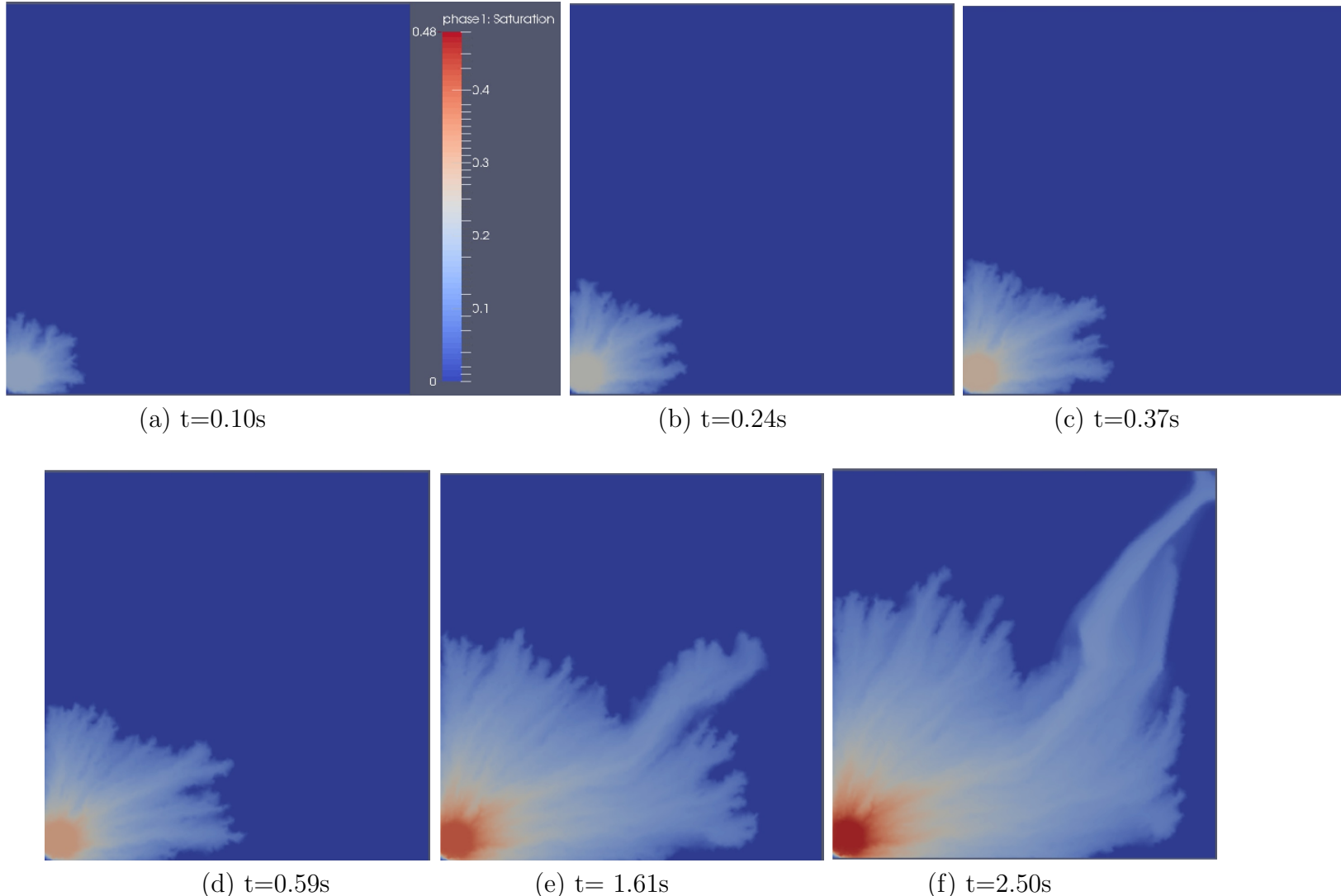


Figure 9: Simulated flow in a modified Hele-Shaw cell with  $VR=150$ : snapshots of saturation profile during 2.50 seconds of simulation. Permeability distribution used in this simulation was the same as shown in Fig. 8a. The domain contains 26313  $P_1$ DG- $P_2$  element-pairs.

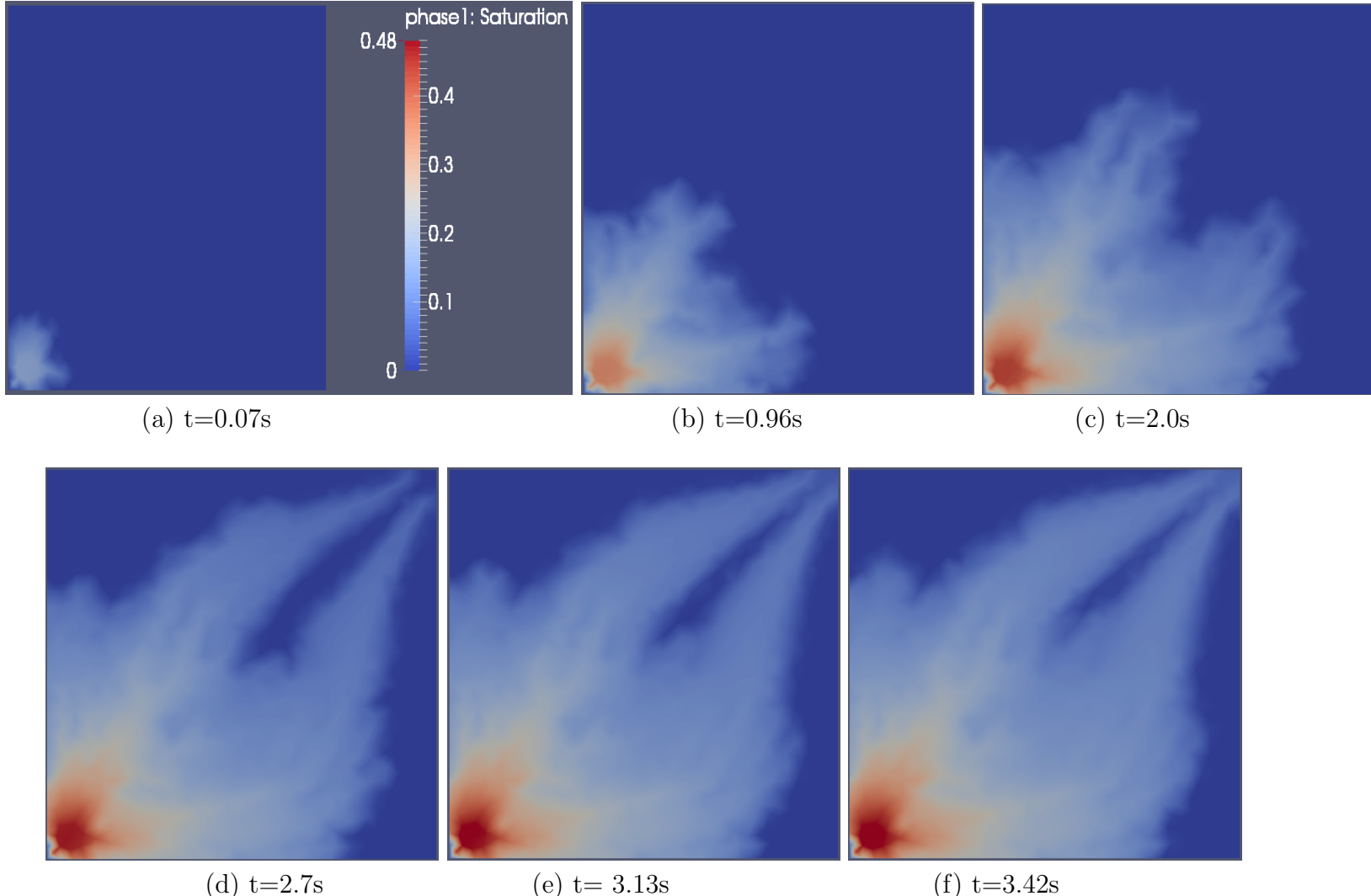


Figure 10: Simulated flow in a modified Hele-Shaw cell with  $VR=150$ : snapshots of saturation profile. Permeability distribution used in this simulation was the same as shown in Fig. 8a. The domain contains 3734 P<sub>1</sub>DG-P<sub>2</sub> element-pairs.

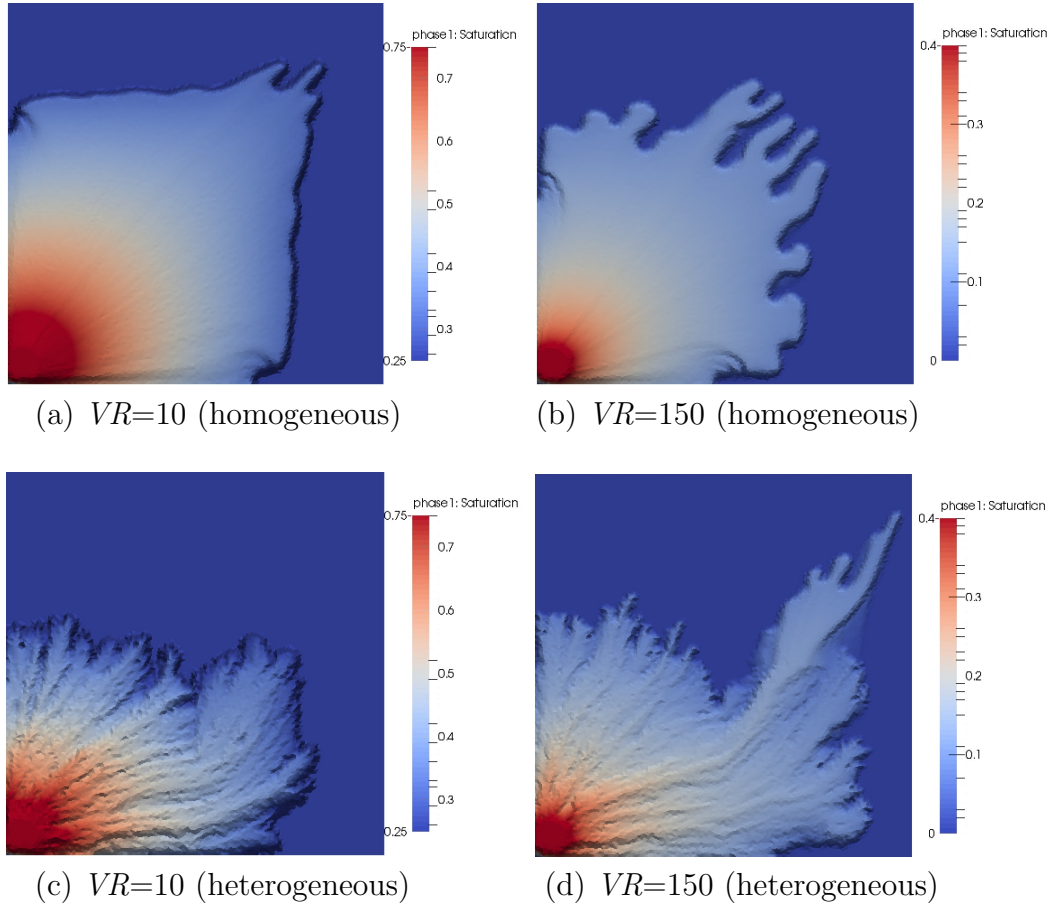
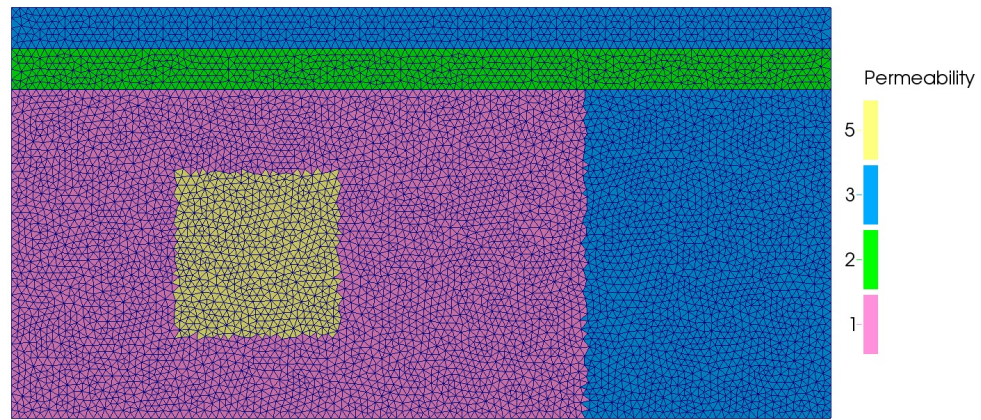


Figure 11: Isosurfaces of simulated flows in Hele-Shaw cells with viscosity ratios of 10 (a and c) and 150 (b and d). Top and bottom rows describe simulations performed with constant *i.e.* *homogeneous with*  $\mathbf{K} = 10^{-10} \text{ cm}^2$  and randomly distributed (*i.e.* heterogeneous, Fig. 8a) permeabilities. Width of largest fingers for homogeneous cases are approximately 0.70 and 0.90cm ( $VR=10$  and  $VR=150$ , respectively), whereas for heterogeneous cases are 0.56 and 0.40cm. Results for homogeneous cases are in good agreement with values obtained from [Guan and Pitchumani \(2003\)](#)'s analytic solution.



(a) Permeability mapping ( $\mathbf{K}$ )



(b) Initial saturation distribution

Figure 12: Impact of mesh resolution on capturing flow instabilities: (a) permeability and (b) initial saturation and mesh resolution used in the simulations performed in Section 4.4. There are 13068  $P_1$ DG- $P_2$  element-pairs in the domain.

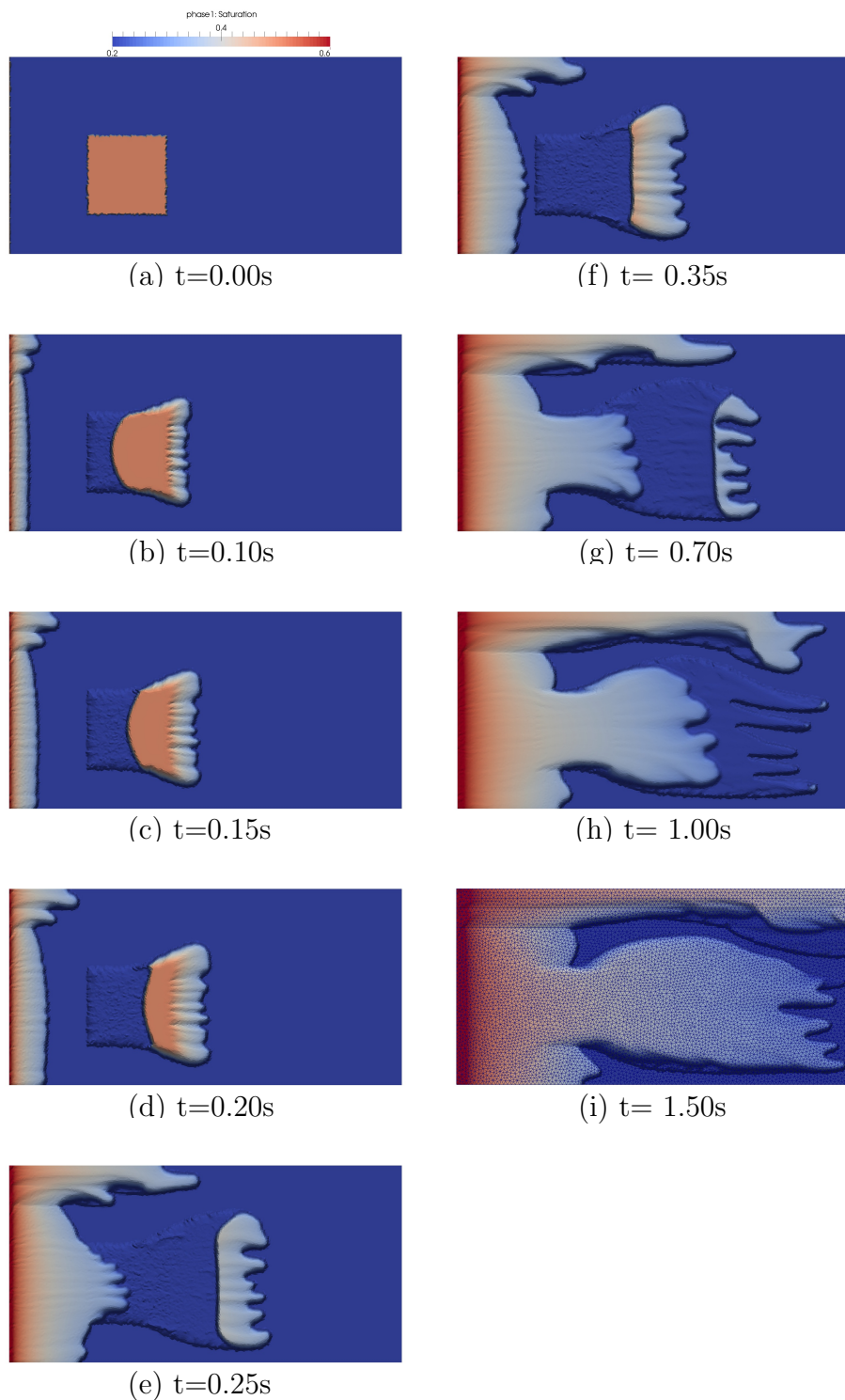


Figure 13: Impact of mesh resolution on capturing flow instabilities: snapshots of saturation field through 1.50 seconds of numerical simulation performed with fixed mesh (of 13068 elements) and  $VR=10$ .

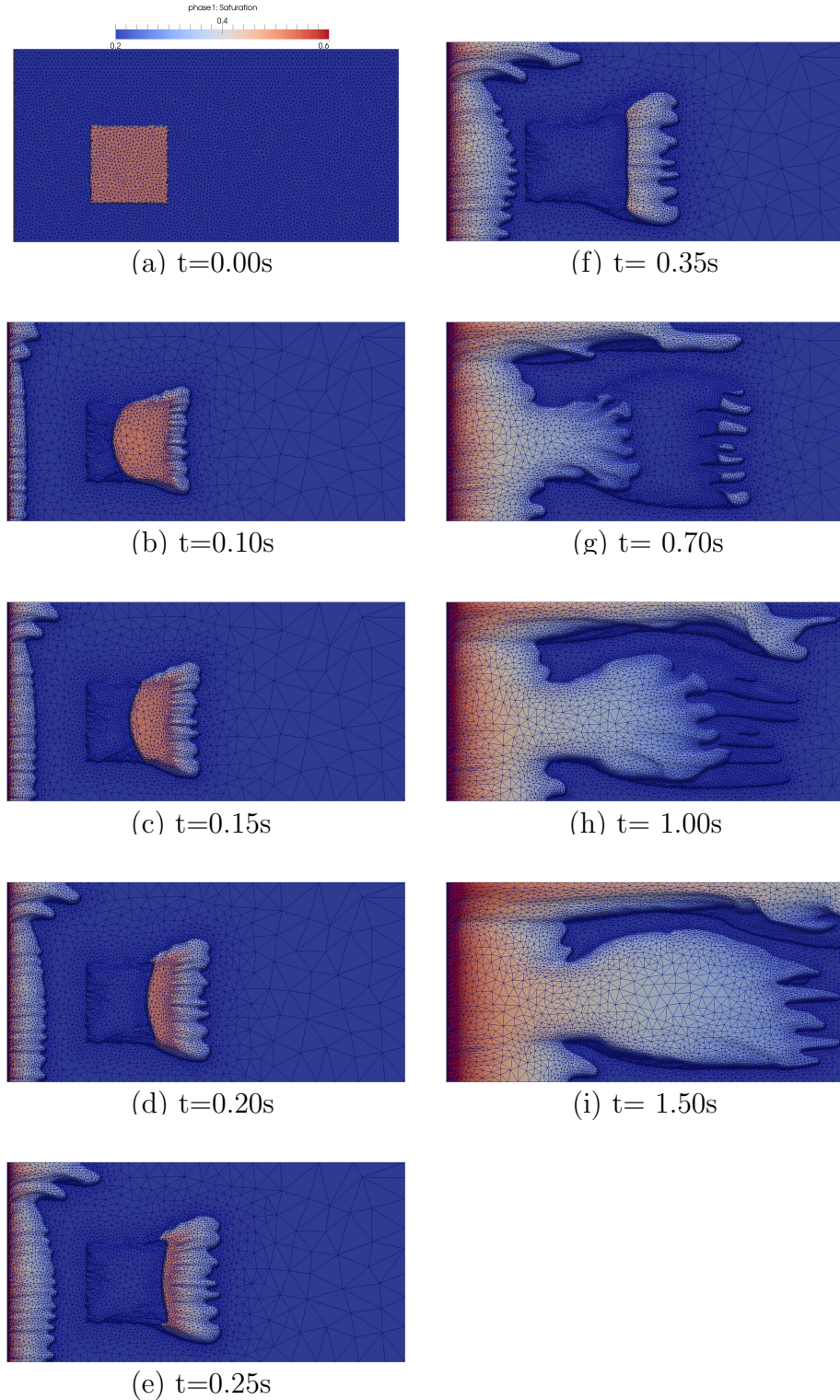


Figure 14: Impact of mesh resolution on capturing flow instabilities: snapshots of saturation field through 1.50 seconds of numerical simulation performed with adaptive mesh and  $VR=10$ .

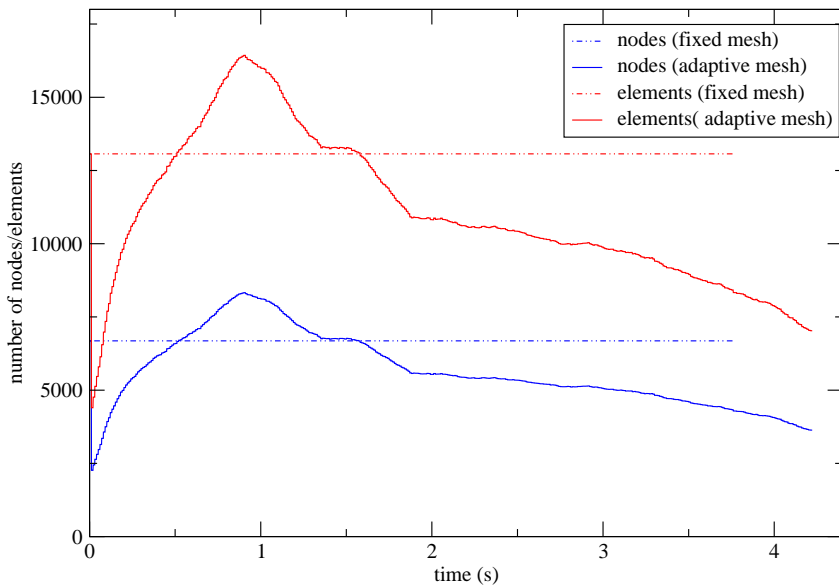
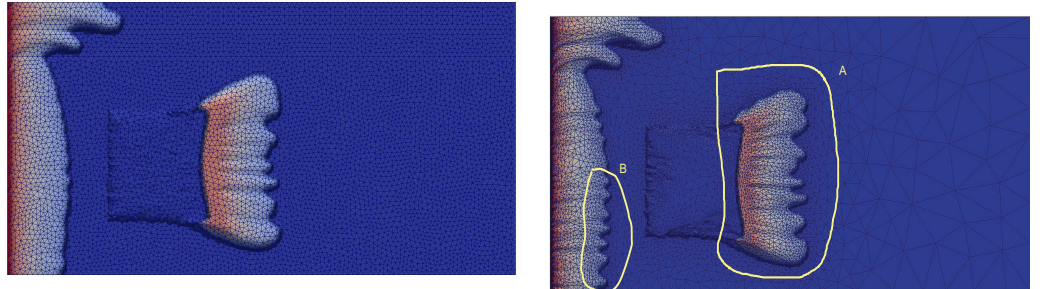
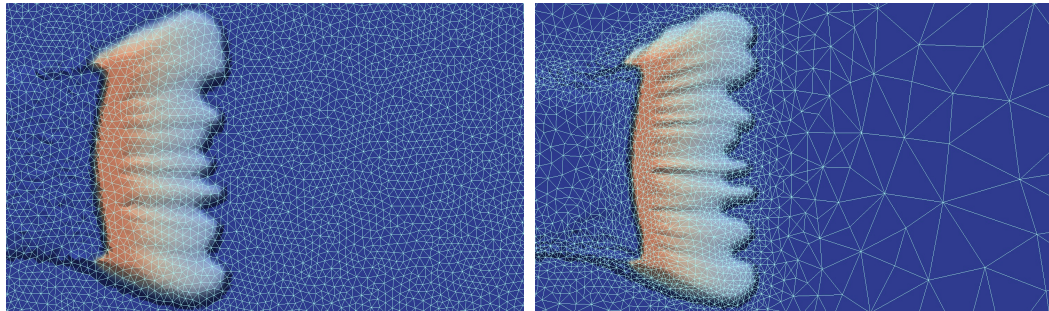


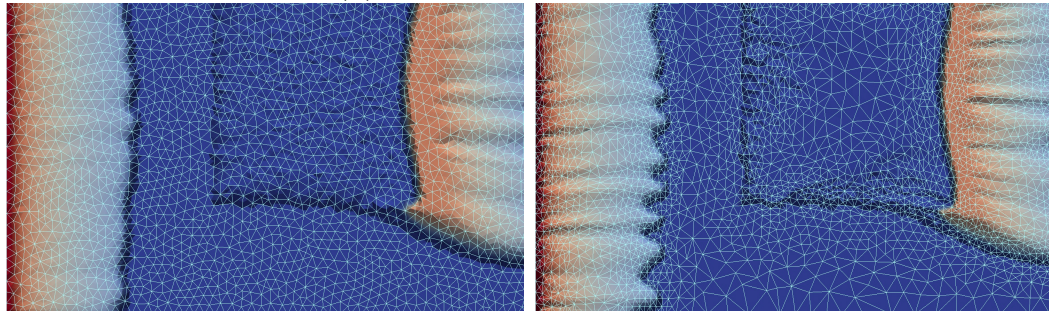
Figure 15: Impact of mesh resolution on capturing flow instabilities: total number of elements and nodes for simulations performed with fixed and adaptive mesh.



(a) fixed and adaptive mesh



(b) Zoom on region *A*



(c) Zoom on region *B*

Figure 16: Impact of mesh resolution on flow instabilities: capturing formation and growth of flow instabilities at fluid interfaces ( $t = 0.20$  s) in two regions of the computational domain, *A* and *B*. Simulations were conducted with fixed (left-hand side) and adaptive meshes.

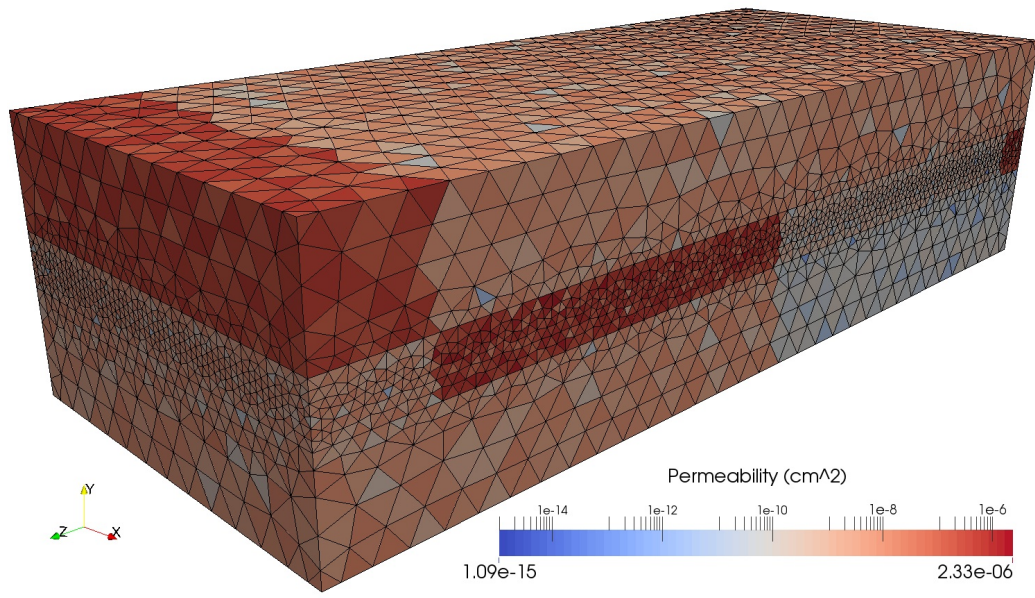


Figure 17: 3D channel flow: permeability distribution. The domain contains 243056 P<sub>1</sub>DG-P<sub>1</sub> element-pairs.

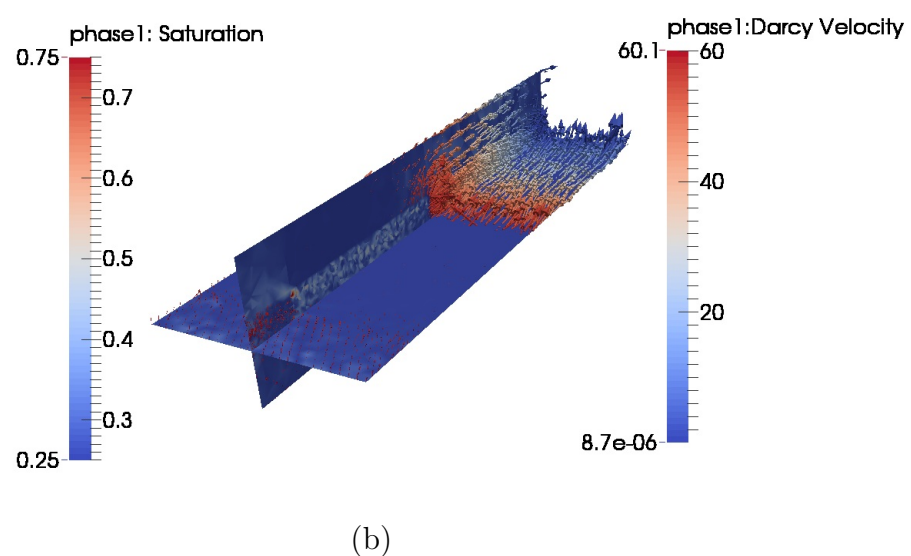
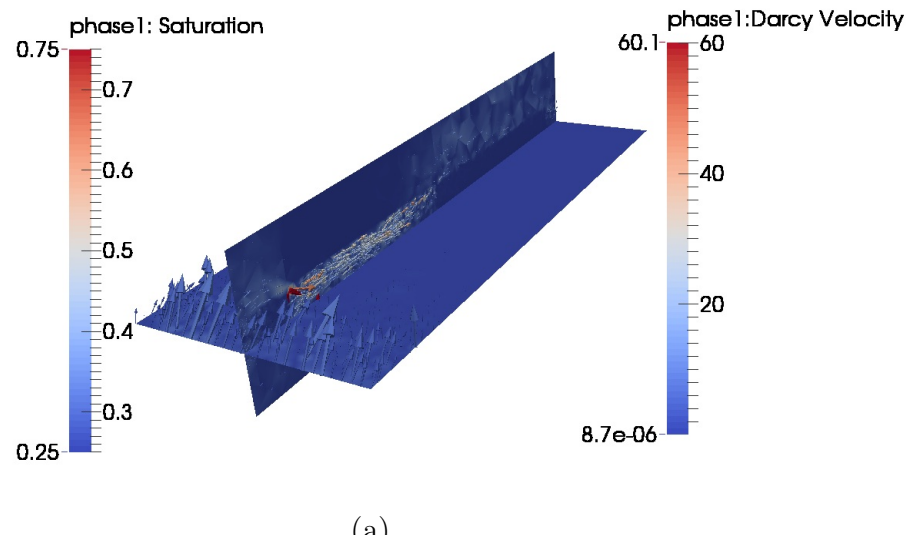


Figure 18: 3D channel flow: XY and YZ planes showing wetting fluid phase Darcy velocity vectors overlapped with wetting fluid saturation at (a)  $t=0.29\text{s}$  and (b)  $t=4.3\text{s}$ .

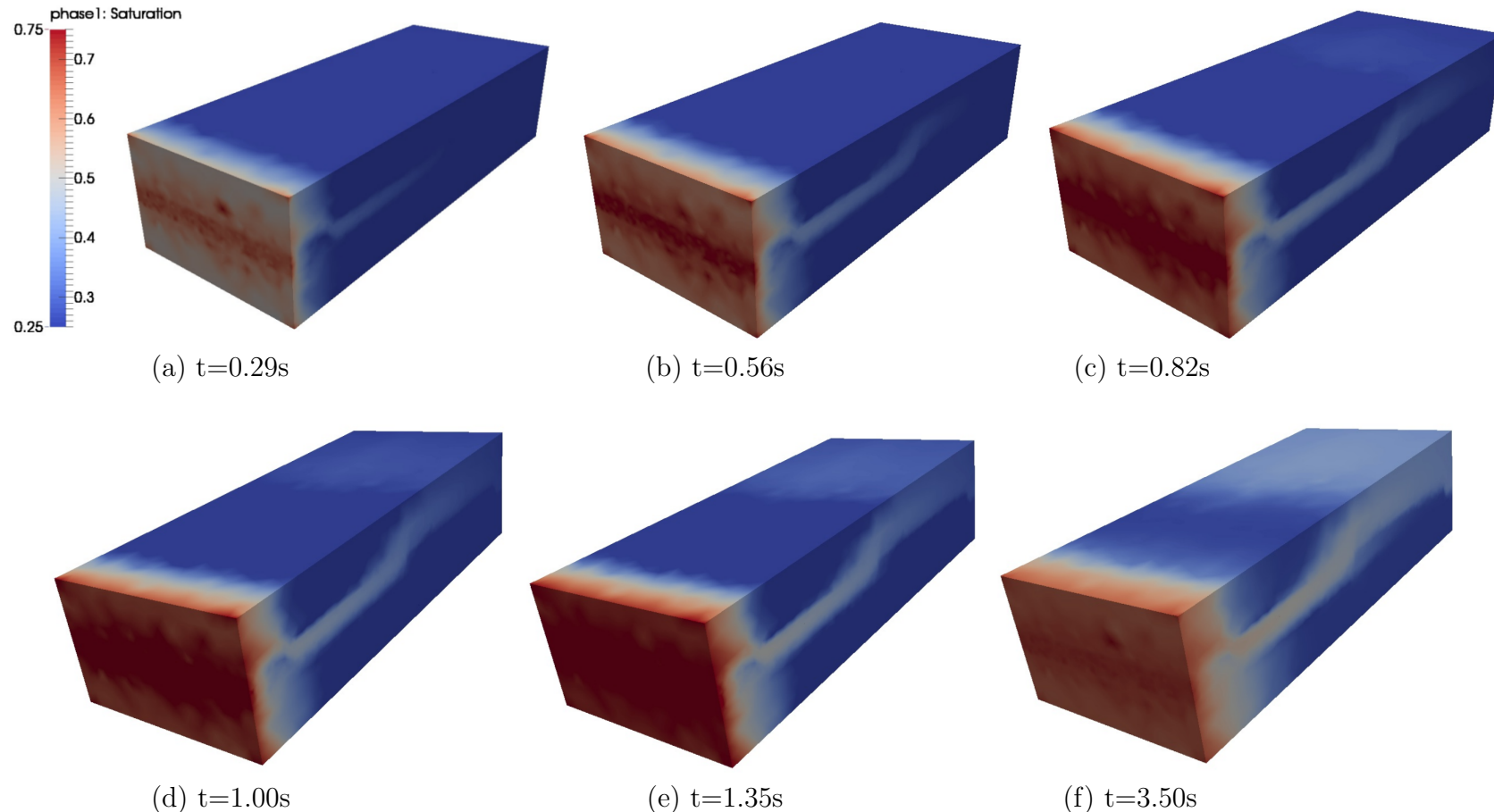


Figure 19: 3D channel flow: saturation front evolving in time and space with preferential flow pathways through 3.50 seconds of numerical simulations. Preferential flow pathway can be readily noticed in these frames, mirroring permeability distribution. The domain contains 368513 P<sub>1</sub>DG-P<sub>1</sub> elements.

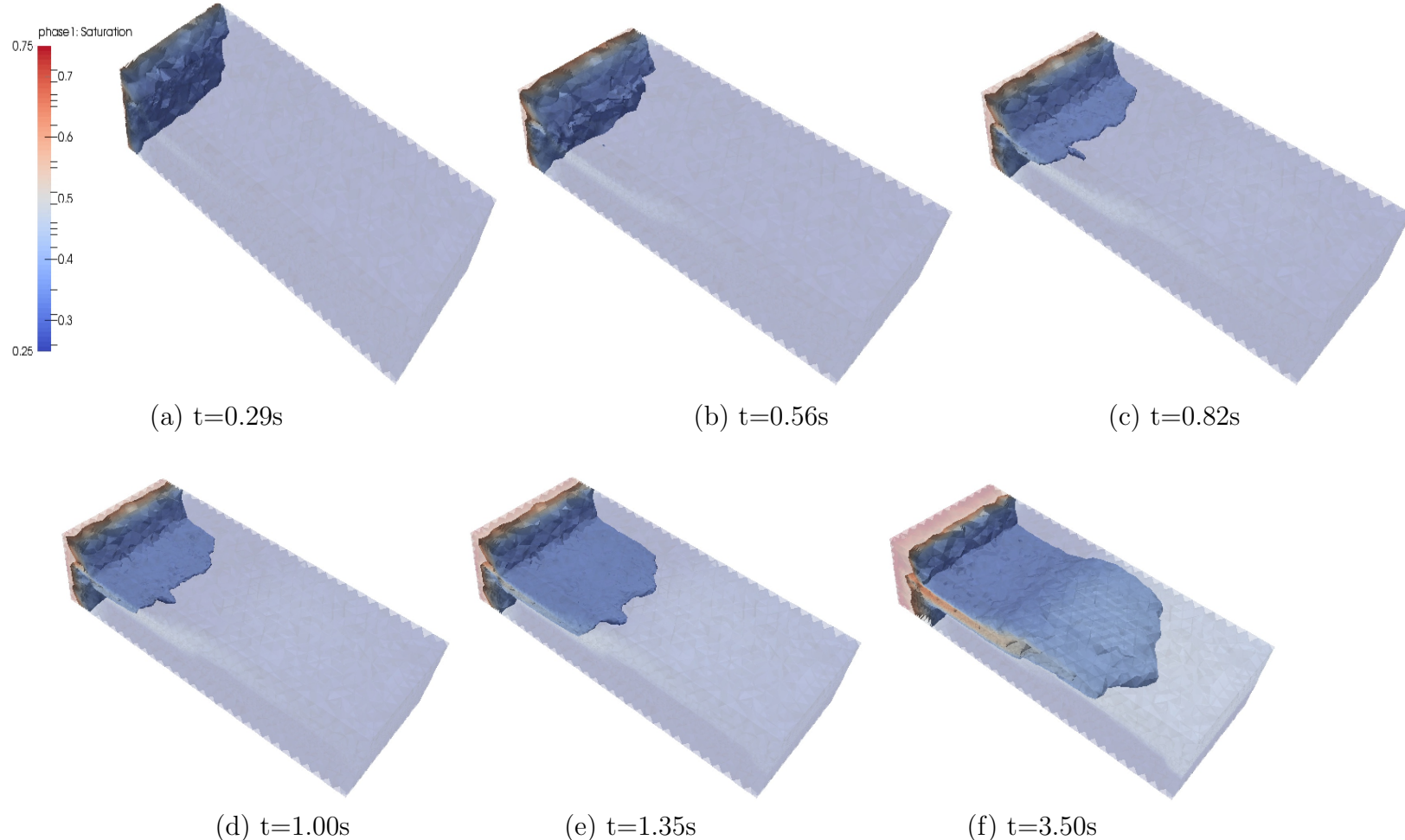


Figure 20: 3D channel flow: Isosurfaces for wetted phase saturation ranging from 0.45 and 0.60 at the same instants of time of Fig. 19. Preferential flow pathway can be readily noticed in (b) and (f). Fingers' formation and growth can be clearly noticed in (b)-(e). The domain contains 368513  $P_1$ DG- $P_1$  elements.

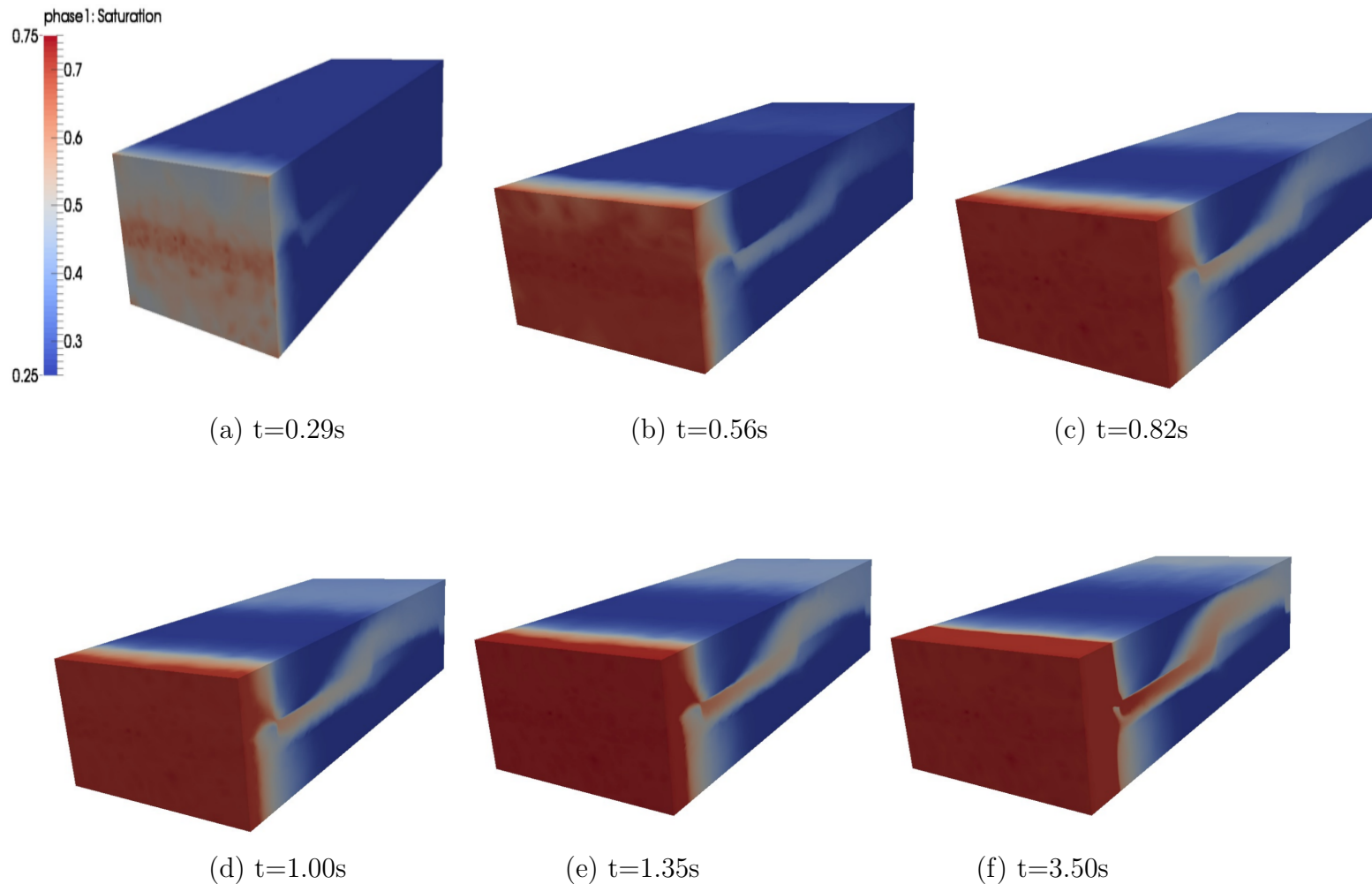
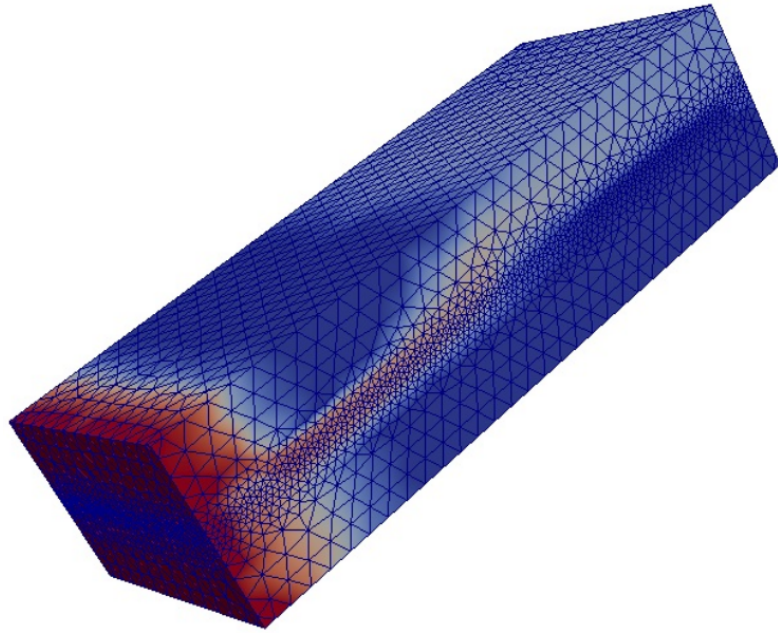
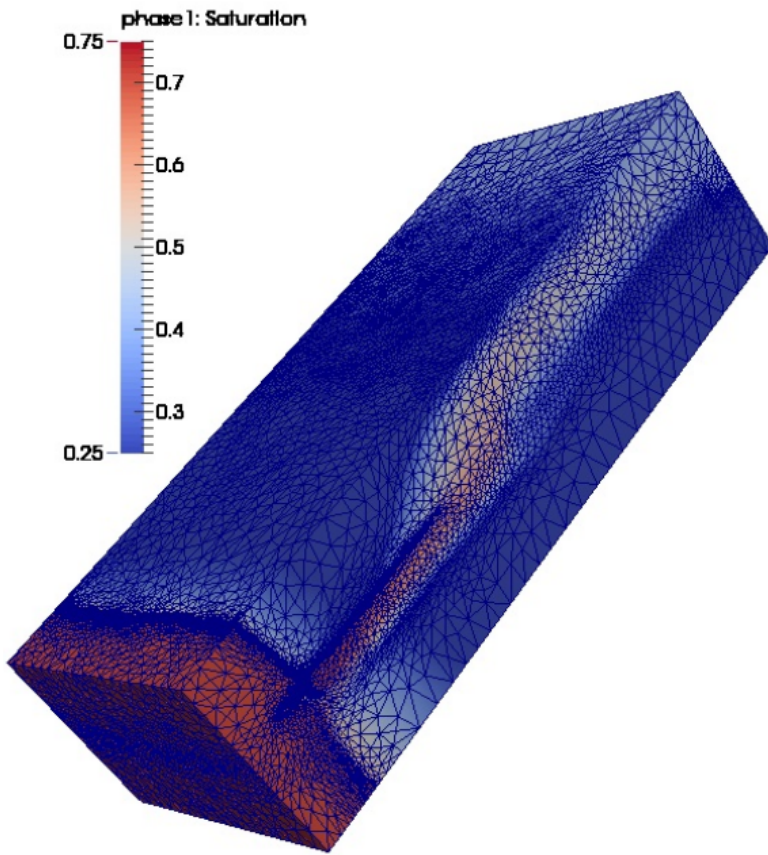


Figure 21: For the same time steps as these are shown in figure 19 there is a description of the same flow path but now using an adaptive and unstructured mesh. The aim was to describe in greater detail the finger patterns, as the flow develops but also address the importance of a resolution, in this case the type of mesh that is used to capture these phenomena.



(a) fixed unstructured mesh of 322493 elements



(b) adaptive and unstructured mesh with a maximum of 1242202 elements at the end of the simulation

Figure 22: This is a qualitative comparison at  $t=\text{end}$  of simulation, for bot the fixed and unstructured mesh used in the 3D domain.

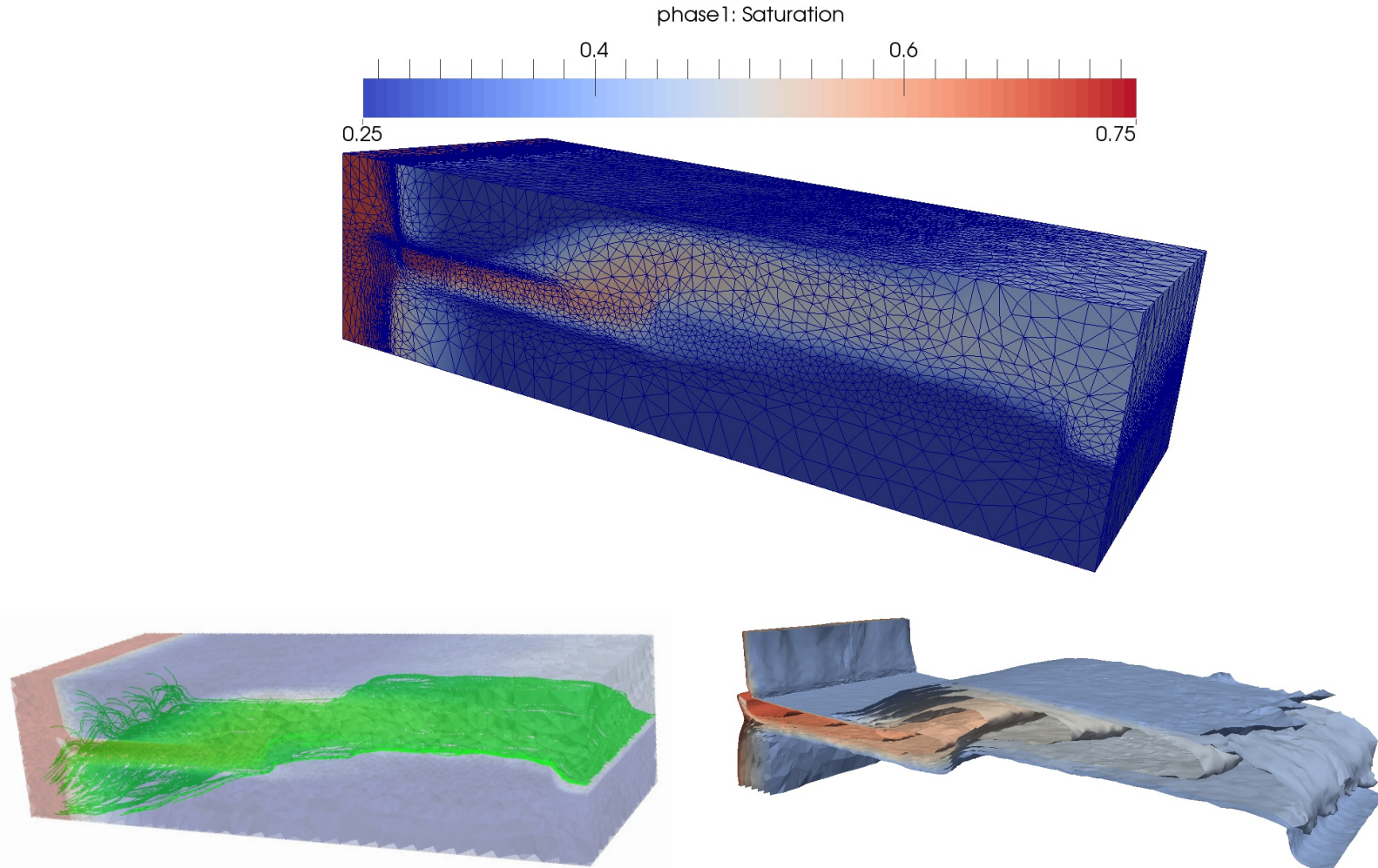


Figure 23: 3D Channel: Text to come

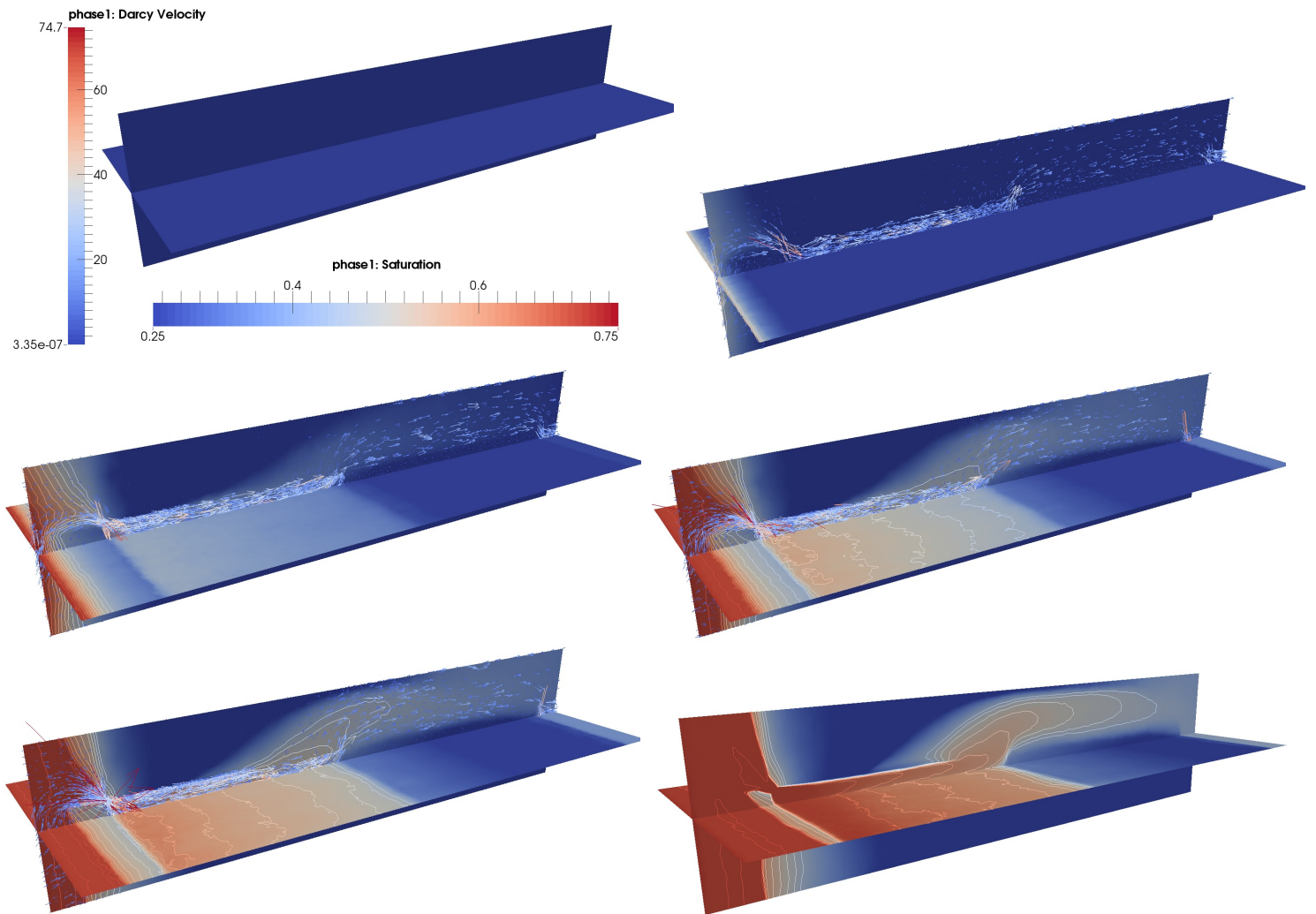


Figure 24: 3D Channel: Text to come **should i mention something here?**